

On the theory of disc photoevaporation

James E. Owen^{1,2*}, Cathie J. Clarke¹ & Barbara Ercolano^{3,4}

¹*Institute of Astronomy, Madingley Road, Cambridge, CB3 0HA, UK*

²*Canadian Institute for Theoretical Astrophysics, 60 St. George Street, Toronto, ON M5S 3H8, Canada*

³*Excellence Cluster Universe, Boltzmannstr. 2, 85748 Garching, Germany*

⁴*University Observatory, Ludwig-Maximilians University Munich, Scheinerstr. 1, 81679 Munich, Germany*

28 August 2018

ABSTRACT

We discuss a hydrodynamical model for the dispersal of protoplanetary discs around young, low mass ($< 1.5 M_{\odot}$) stars by photoevaporation from the central object's energetic radiation, which considers the far-ultraviolet as well as the X-ray component of the radiation field. We present analytical scaling relations and derive estimates for the total mass-loss rates, as well as discussing the existence of similarity solutions for flows from primordial discs and discs with inner holes. Furthermore, we perform numerical calculations, which span a wide range of parameter space and allow us to provide accurate scalings of the mass-loss rates with the physical parameters of the systems (X-ray and FUV luminosity, stellar mass, disc mass, disc temperature and inner hole radius).

The model suggest that the X-ray component dominates the photoevaporative mass-loss rates from the inner disc. The mass-loss rates have values in the range from 10^{-11} to $10^{-7} M_{\odot} \text{ yr}^{-1}$ and scale linearly with X-ray luminosity, with only a weak dependence on the other parameters explored. However, in the case of high FUV to X-ray ($L_{\text{FUV}}/L_{\text{X}} > 100$) luminosity ratios, the FUV constricts the X-ray flow and may dominate the mass-loss.

Simulations of low mass discs with inner holes demonstrate a further stage of disc clearing, which we call ‘thermal sweeping’. This process occurs when the mid-plane pressure drops to sufficiently low values. At this stage a bound, warm, X-ray heated region becomes sufficiently large and unstable, such that the remaining disc material is cleared on approximately dynamical time-scales. This process significantly reduces the time taken to clear the outer regions of the disc, resulting in an expected transition disc population that will be dominated by accreting objects, as indicated by recent observations.

Key words:

accretion, accretion discs - circumstellar matter - planetary systems: protoplanetary discs - stars: pre-main-sequence - X-rays: stars.

1 INTRODUCTION

The evolution and dispersal of protoplanetary discs is an important step in the star and planet formation process. Protoplanetary discs provide the material from which planets form, implying that the initial evolution of newly formed planets is coupled to the properties of the parent disc. Moreover the disc dispersal time-scale ultimately sets the time in which (gas) planets must form.

It is observationally well established that at an age of 1 Myr most stars are surrounded by discs that are optically thick at infra-red (IR) wavelengths, which have in most cases

disappeared by typical ages of 10 Myr (e.g. Haisch et al. 2001, Mamajek 2009). Optically thick discs around young stars evolve in a manner that is consistent with ‘standard’ viscous evolution theory, where the disc diagnostics decline with time in an approximately power law fashion (Hartmann et al. 1998). However, the final evolution from disc-bearing (primordial) to disc-less status appears to be much more rapid than viscous theory predicts (e.g. Luhman et al. 2010; Muzerolle et al. 2010; Ercolano et al. 2011) and to occur over the entire range of disc radii probed by IR observations. Furthermore, given that the sub-millimetre observations show that most non-accreting stars (WTTs) are devoid of emission out to several hundreds of AU (Duvert et

* E-mail: jowen@cita.utoronto.ca

al. 2000, Andrews & Williams 2005, 2007), the clearing must be correlated across all disc radii from 1AU to 100AU.

Further clues regarding the mechanism for clearing discs are provided by objects which have been identified as ‘transition’ discs. These are discs which show a deficit in opacity at near-IR (NIR) wavelengths compared to a standard optically thick ‘primordial’ disc, but are consistent with standard optically thick discs at Mid-IR/Far-IR (MIR/FIR) wavelengths; furthermore some of these objects show small NIR excesses above the photosphere (not consistent with a primordial disc) have been labelled as ‘pre-transition’ discs (e.g. Espaillat et al. 2010; Furlan et al. 2011). Such spectral characteristics are most readily explained in terms of a hole or gap in the dust in the inner regions of the disc. However, there is no clear consensus as to the origin of such structures and the debate is complicated by the fact that they display a wide variety of other observational characteristics: for example some show evidence for accretion (e.g. Calvet et al. 2005, Najita et al. 2007, Hughes et al. 2009) while others do not (Cieza et al. 2010; Merin et al. 2010); there is also evidence in some systems that the deficit in opacity at NIR wavelengths does not necessarily preclude significant quantities of gas and small amounts of dust in the inner disc (Espaillat et al. 2010) although this is not always the case (Calvet et al. 2002). The frequency of these ‘transition/pre-transition’ discs compared to those of primordial discs suggest that approximately 10-20% of discs are in this stage (Strom et al. 1989, Skrutskie et al. 1990, Luhman et al. 2010, Ercolano et al. 2011a; Furlan et al. 2011). Assuming that these objects are in transition from a primordial to a fully cleared state, this observation provides two important constraints: the transition time from primordial to cleared is approximately 10% of the discs total lifetime, and that the clearing process proceeds from the inside out.

While many theories have been developed in order to explain the observations of ‘transition’ discs: grain growth (Dullemond & Dominiki, 2005); photophoresis (Krasuss et al. 2007); MRI-driven winds (Suzuki & Inutsuka, 2009), only two mechanism have been proposed that can explain the observations of ‘transition’ discs in the context of total (gas & dust) disc clearing (assuming that indeed all discs pass through a ‘transition’ disc phase). These are photoevaporation (e.g. Clarke et al. 2001) and planet formation (e.g. Armitage & Hansen, 1999). Photoevaporation and planet formation are processes which compete to remove gas from the disc, and it is still a matter for debate whether one process dominates over the other. Ercolano & Clarke (2010) discuss the implications of metallicity on both processes and Yasui et al. (2009) provide very preliminary observations of smaller disc frequencies in low metallicity regions in the extreme outer Galaxy, consistent with the predictions from X-ray photoevaporation models and arguing against planet formation as a main dispersal mechanism.

Like any theory, the photoevaporation model has progressed through several stages of evolution, with the original theories only including photoevaporation without viscous disc evolution (Shu et al. 1993; Hollenbach et al. 1994; Yorke & Welz 1996; Richling & Yorke 1997), or photoevaporation from external sources (Johnstone et al. 1998; Richling & Yorke 1998; Richling & Yorke 2000; Adams et al. 2004). It was Clarke et al. (2001) who realised that mass-loss from the surface of a disc due to heating (photoevaporation), coupled

with viscous evolution results in a gap opening in the inner disc when the photoevaporation rate and accretion rate become comparable. The inner disc then drains onto the central star on its own much faster local viscous time-scale. While the basic ideas have remained identical (photoevaporation and viscous process compete until photoevaporation eventually opens a gap in the inner disc which then rapidly drains on to the central star), the actual calculations of the photoevaporation rates have progressed greatly. The original model used semi-analytic mass-loss rates due to EUV radiation calculated by Hollenbach et al. (1994), while later the photoevaporative flow was modelled hydrodynamically by Font et al. (2004). In these models the disc is mainly irradiated by a diffuse field of recombination photons from the atmosphere of the inner disc. Subsequently Alexander et al. (2006a) realised that, following the draining of the inner disc, the inner-edge of the hole is instead directly exposed to the radiation field from the star; this results in higher mass-loss rates which rapidly clear the remaining disc out to large radii (Alexander et al. 2006b).

Recently, a lot of attention has been paid to other high energy radiation fields; X-rays (Alexander et al. 2004, Ercolano et al. 2008, 2009, Owen et al. 2010, 2011b) and FUV (Gorti & Hollenbach 2008, 2009; Gorti et al. 2009). These calculations have yielded much higher photoevaporation rates than the original EUV rate. These higher mass-loss rates primarily arise from significant mass-loss at larger radii in the disc ($R > 10$ AU), due to the ability of the FUV and X-rays to heat much larger columns of gas to of order the escape temperature. While the central star certainly produce significant fluxes of FUV, EUV and X-rays (e.g. Alexander et al. 2005, Ingleby et al. 2011) it is important to determine which, or which combination of high energy rates are responsible for setting the photoevaporation rate.

Some of the main observational tests of photoevaporation are based on observational statistics of disc populations as a function of time. Owen et al. (2011b) showed that the X-ray photoevaporation model is consistent with the current diagnostics of disc evolution, and made some predictions about how these diagnostics should correlate with X-ray luminosity. Furthermore, Drake et al. (2009) reported that accretion rate measurements and X-ray observations in Orion, point to a process of X-ray driven ‘photoevaporation-starved accretion’, where higher mass-loss rates prevent material accreting onto the central star, leading to lower accretion rates. This process was theoretically demonstrated by Owen et al. (2011b) and is also likely to explain the systematic discrepancy between the X-ray luminosities of accreting and non-accreting young stars. Unlike the previous EUV models (e.g. Alexander et al. 2006b; Alexander & Armitage, 2009), the X-ray photoevaporation model can account for a large fraction of the observed ‘transition’ discs. In particular, photoevaporation can account for the population of small inner holes $R < 20$ AU, those with low accretion rates $\dot{M}_* < 10^{-8} M_\odot \text{ yr}^{-1}$ and those with gas inside the inner-hole. However, ‘transition’ discs with large inner holes and large accretion rates are likely to be created through a different mechanism (e.g. Espaillat et al. 2010).

The first direct evidence and best test of individual photoevaporation models is the detection of a blue-shifted 12.8 μm NeII line from the surface of the disc around TW Hya (Pascucci & Sterzik 2009), which is consistent with ei-

ther an EUV or X-ray driven photoevaporative wind (Pascucci et al. 2011). Moreover, Ercolano & Owen (2010) recently showed that the previously unexplained low velocity component of the OI 6300Å, - emission blue-shifted by $\sim 5\text{km s}^{-1}$ detected by Hartigan et al. 1995 around most primordial discs - is naturally produced in an X-ray driven photoevaporative flow. The observed luminosity is too high to be consistent with an EUV wind and the blue-shift is too large to be consistent with an FUV wind. Currently, the only well resolved OI 6300Å line is detected from the accreting ‘transition’ disc around TW Hya, where the line presents with no blue-shift (Pascucci et al. 2011). Unfortunately, hydrodynamic models of the inner regions of photoevaporating transition discs during the accreting phase do not exist for any of the photoevaporation models (only transition discs with cleared inner gas discs were considered by Ercolano & Owen 2010) and useful comparisons must wait until these calculations are completed. Therefore, pending these calculations, and the availability of high resolution spectroscopic observations of many objects, direct comparisons of predicted to observed OI line profiles are not possible.

While observations are providing a fruitful avenue for direct comparisons of photoevaporation models, in this work we develop a theoretical framework in which we can analyse the combined effects of all three heating mechanisms (EUV, FUV and X-rays). The most relevant scale in any photoevaporation model is the radius at which a gas of a given temperature (T_{gas}) becomes unbound from the central star and is given by¹:

$$r_g = 8.9\text{AU} \left(\frac{T_{\text{gas}}}{10^4 \text{K}} \right)^{-1} \left(\frac{M_*}{1 M_\odot} \right) \quad (1)$$

For the EUV photoevaporation model this becomes a fixed radius (for a given disc), since EUV heating gives rise to essentially isothermal gas at 10^4K . For the X-ray and FUV model it is better to think of this radius as an escape temperature scaled length, allowing the consideration of different radial scales around different mass stars. However, in order to be consistent with the previous EUV only literature (Hollenbach et al. 1994; Clarke et al. 2001; Font et al. 2004; Alexander et al. 2006a), we separately fix $R_g = 8.9(1/M_\odot)\text{AU}$. Furthermore, as we will discuss in detail in Section 2, this radius has an important physical significance as it is a measure of the radius at which a flow at temperature T_{gas} can go through the sonic surface. For X-ray heating in the range $T_{\text{gas}} \sim 1000 - 10000\text{K}$, $r_g \sim 1 - 10\text{AU}$ for a very low mass star ($0.1M_\odot$) and $r_g \sim 10 - 100\text{AU}$ for a solar type star. For FUV heating, $T_{\text{gas}} \lesssim 1000\text{K}$, $r_g \gtrsim 10\text{AU}$ for a very low mass star and $r_g \gtrsim 100\text{AU}$ for solar type stars.

In this work, we lay out the theoretical foundation for photoevaporation, deriving the scaling with X-ray luminosity and stellar mass in Sections 2. In Section 3 we discuss the likely interplay between the effects of combined EUV, FUV and X-ray heating on the calculation of photoevaporation rates. Section 4 presents the results of radiation-hydrodynamic calculations that test the theoretical foundations laid out in the Section 2, while Section 5 contains some

simple numerical experiments that address the discussion of combined FUV and X-ray heating contained in Section 3. Section 6 describes the final clearing of the outer disc by ‘thermal sweeping’. In Section 7 we describe the implications of photoevaporation on disc evolution and dispersal. In Section 8 we discuss the presented results and draw our conclusions in Section 9.

In Appendix A we discuss the possibility of self-similarity in X-ray heated flows and in Appendix B we provide numerical fits to our photoevaporation calculations for use by the community.

2 THE THEORY OF X-RAY PHOTOEVAPORATION

The problem of thermally driven winds from discs has been studied analytically in the past (Begelman et al. 1983; Liffman 2003; Adams et al. 2004). While a full analytic solution to the problem has not been obtained in even the most simplistic thermodynamic constructions, considerable progress can still be made. In the Appendix we discuss the existence of similarity solutions with regard to the problem of X-ray photoevaporation. The results from the analysis are as follows:

- For primordial discs, the total mass-loss rates scale linearly with X-ray luminosity and are independent of stellar mass.
- For primordial discs, the density at a given value of \mathbf{r}/R_g scales with X-ray luminosity and stellar mass as $n(L_X, M_*) \propto L_X M_*^{-2}$ for primordial discs.
- For discs with inner holes of fixed radius, the total mass-loss scales linearly with the X-ray luminosity.
- Discs with inner holes with a range of radii are not strictly mutually self-similar: see section 4.3.1 for an approximate self-similarity argument that can be used to understand the numerical results in this case.

In this section, we derive the scalings listed above using a series of simple analytic arguments. Since the mass-flux is conserved in any steady-state photoevaporative flow we are free to evaluate this quantity at any point in the flow. Therefore, choosing to do this at the sonic surface the total mass-loss rate is given by:

$$\dot{M}_w = \int_S n_s(\mathbf{r}_s) c_s(\mathbf{r}_s) \mathbf{l}(\mathbf{r}_s) \cdot d\mathbf{S} \quad (2)$$

where S is the sonic surface, n_s & c_s are the density and sound speed at the sonic surface respectively, and \mathbf{l} is the unit vector along a streamline. In the case of a flow from a disc, this can be approximately written as:

$$\dot{M}_w = 2 \int_0^\infty 2\pi R n_s(R) c_s(R) dR \quad (3)$$

where we note that the true mass loss flux will differ from this by a factor of order unity due to the fact that the flow is not purely vertical at the sonic surface. Therefore, provided we can determine the flow properties at the sonic surface we can estimate the total mass-loss rates.

¹ Throughout this work we use $\{R, \phi, z\}$ to represent the cylindrical co-ordinate system and $\{r, \theta, \varphi\}$ to represent the spherical co-ordinate system, in all cases centred on the star.

2.1 The Sonic Surface in X-ray Heated Flows

The sonic point is a critical point of the steady-state momentum equation when $u = c_s$, and physically arises as a consequence of wave-steepening requirements, namely that no strong shock forms (Landau & Lifshitz, 1987).

Several authors have derived the conditions on the sound speed at the sonic surface for a flow emerging from a disc (e.g. Begelman et al. 1983; Adams et al. 2004; also shown in Appendix A for completeness). Under the conditions expected for disc winds (sub-sonic launching, flow time-scale $>$ thermal time-scale, height of the sonic surface (z_s) $\gg R$) the sound speed at the sonic surface should be to order unity the Parker value at each cylindrical radius, namely:

$$c_s^2 \approx \frac{GM_*}{2R} \quad (4)$$

Therefore, we can *a priori* determine the sound speed, and hence the temperature at the sonic surface.

2.1.1 Density-Sound-Speed Coupling in X-ray Heated Flows

If we can specify both the density and sound speed at the sonic surface then we have determined the mass-flux in the entire flow as mass-flux is conserved. We argued above that in the case of disc winds, the sound speed at the sonic surface is roughly given by the Parker value (Equation 4). This means that the gas temperature at the sonic surface is also simply given as a function of cylindrical radii.

It is well known that the temperature of X-ray heated gas can be described in terms of the local ionization parameter (e.g. Tarter et al. 1969), given by:

$$\xi = \frac{4\pi F_X}{n} \quad (5)$$

where F_X is the X-ray flux ($L_X/4\pi r^2$). Ercolano et al. (2009ab) & Owen et al. (2010) found that the temperature of gas within a column density to the central star of 10^{22} cm $^{-2}$ (this being the penetration depth of 1 KeV photons 2) to the central star can be described in terms of optically thin X-ray heating. Thus, adopting the assumption of optically thin X-ray heating the ionization parameter becomes $\xi = L_X/nr^2$, and the gas temperature is specified in terms of local variables only, where the form of this profile $T = f(\xi)$ is shown in Figure 1.

At the sonic surface (provided $z_s \gg R$ so $R \sim r$) we may write:

$$c_s^2 = \frac{k_B f(L_X/n_s R^2)}{\mu m_h} = \frac{GM_*}{2R} \quad (6)$$

Therefore, we may re-arrange Equation 6 to give an expression for the density at the sonic surface 3 :

$$n_s = \frac{L_X}{R^2} \left[f^{-1} \left(\frac{GM_* \mu m_h}{2k_B R} \right) \right]^{-1} \quad (7)$$

2 see discussion in Section 4.2.2 for implications of attenuation which is neglected here

3 where $f^{-1} \circ f = 1$ and $f^{-1} \neq 1/f$

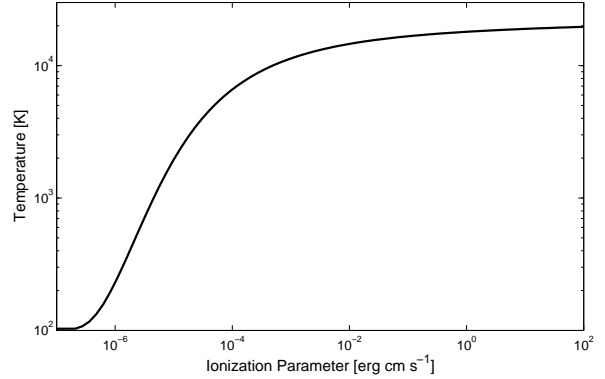


Figure 1. Fit to temperature-ionization parameter calculated by Owen et al. (2010).

One may also write this at fixed R/R_g to obtain the mass-scaling of the density, namely $n \propto M_*^{-2}$. Thus, provided we know the form of $f(\xi)$, the density at the sonic surface is also fixed *a priori* through the temperature-ionization parameter relation, which provides a density-sound-speed coupling.

2.1.2 Consequences of Density-Sound-Speed Coupling

The density-sound-speed coupling found at the sonic surface in optically thin heated X-ray heated flows provides some very powerful constraints on the flow properties of X-ray photoevaporative winds, and implies that the structure and temperature of the underlying disc has little effect on the resulting flow.

This arises since in any steady state flow mass-flux must be conserved; therefore, in this case since we are able to described the mass-flux at the sonic surface *a priori* with reference to the X-ray physics alone, we have determined the mass-flux in the *entire* flow without reference to the disc properties.

This picture is very different to pure EUV (Hollenbach et al. 1994) or FUV (Gorti & Hollenbach 2008,2009) flows where the underlying density structure in the launch region is crucial to the mass-loading of the flow. Unlike EUV/FUV flows where the flow will adjust to changes in the underlying disc's structure, an X-ray flow will adjust the underlying disc structure to 'feed' the flow at the required rate, provided the sonic surface remains optically thin to the X-rays responsible for the heating.

2.2 Estimates of the total mass-loss rate

Armed with the knowledge that it is the X-ray physics, and not the disc structure that sets the overall mass-loss rates we are free to integrate Equation 3 over the sonic surface to estimate the total mass-loss rates. We can use Equations 4 & 7 to substitute for n_s and c_s in the integrand. Furthermore, if we change the variable of integration in Equation 3 from

cylindrical radius R to escape temperature we find:

$$\dot{M}_w(M_*, L_X) = L_X \sqrt{\frac{8k_B \pi^2}{\mu m_h}} \int_0^\infty dT_{\text{esc}} \frac{T_{\text{esc}}^{-1/2}}{f^{-1}(T_{\text{esc}}/2)} \quad (8)$$

$$\approx 8 \times 10^{-9} \left(\frac{L_X}{1 \times 10^{30} \text{ erg s}^{-1}} \right) M_\odot \text{ yr}^{-1} \quad (9)$$

(where the second result comes from evaluating the integral out to an escape temperature of 1000K, or a radius of $\mathcal{O}(100)$ AU for a solar mass star). This mass-loss rate is in good agreement with the numerical result of $6.7 \times 10^{-9} M_\odot \text{ yr}^{-1}$ obtained from the hydrodynamic simulations of Owen et al. (2011b) and is also consistent with the approximately linear scaling between mass-loss rate and X-ray luminosity found in the simulations. Furthermore, the results indicates there is no explicit dependence between stellar mass and mass-loss rate (although the $M_* - L_X$ scaling introduces a strong positive implicit scaling). We also derive this scalings in more detail through the existence of similarity solutions presented⁴ in Appendix A.

2.3 Importance of Numerical Results

In Sections 4 and 5 we present hydrodynamical simulations that have been designed to test and refine the ideas set out above. However, the role of the numerical simulations is not merely one of validation: although Equation 9 is of great utility in predicting the integrated mass-loss from the system (and can be used to derive the mass loss rate per unit area *at the sonic surface*), it does not - without knowledge of the detailed streamline topology below the sonic surface - allow one to calculate the mass loss rate per unit area from the disc itself ($\dot{\Sigma}_w(R)$). For example the form of the integrand in Equation 9 suggests that the mass-loss is dominated in the lower temperature regime (2000-5000K), but these stream-lines connect the sonic surface to the disc surface in a non-uniform way, such that there is not a one to one correspondence between the mass-flux profile at the sonic surface and the mass-flux profile from the disc. This results in a mass-loss profile that peaks at smaller radii in the disc, rather than the large radius suggested by the calculations at the sonic surface. Although this may appear to be a detail, it turns out that, when photoevaporation is combined with secular disc evolution, the pattern of disc clearing is rather sensitive to the form of $\dot{\Sigma}_w(R)$. In particular, it is the form of $\dot{\Sigma}_w(R)$ that determines where the gap first opens in the disc, the extent to which the system undergoes a period of ‘photoevaporation-starved accretion’ prior to gap opening and hence the surface density profile of the disc outside the gap. This latter then determines the rate at which the disc is evaporated once the inner disc is completely cleared out. This is of obvious importance if one wants to compare the predictions of photoevaporation theory with the observed incidence of transition discs with holes of different sizes (see Section 8.1).

⁴ Note that the scalings presented in Appendix A do not rely on the approximate expression for the temperature at the sonic surface contained in Equation 4.

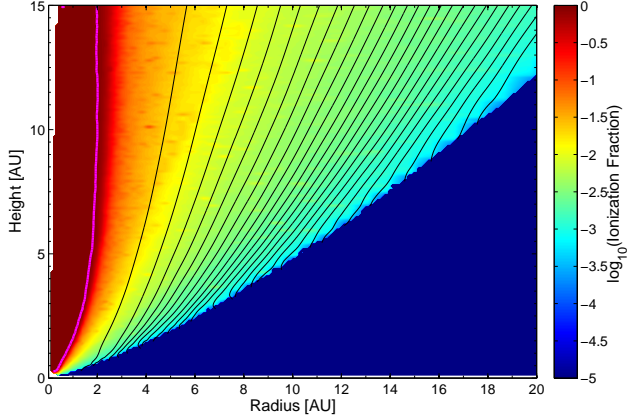


Figure 2. Ionization structure of the X-EUV wind around a $0.7 M_\odot$ star with an X-ray luminosity of $2 \times 10^{30} \text{ erg s}^{-1}$, the streamlines are equispaced in 2% of the cumulative mass-loss rate and the magenta contour shows the region of 98% ionization fraction (i.e. roughly the penetration depth of EUV photons). This shows that an X-ray driven wind is itself entirely optically thick to EUV photons and prevents them from reaching the disc surface

3 THEORY OF UV & X-RAY PHOTOEVAPORATION

We now turn to considering the situation where X-ray heating is combined with ultraviolet heating, considering in turn the case the ionising (EUV) and non-ionising (FUV) continua.

3.1 EUV and X-ray heated flows

The radiative transfer calculations of Ercolano & Owen (2010) demonstrated why, in the presence of an X-ray flow, EUV heating can be neglected. Figure 2 shows the ionization structure of an X-ray wind subject to combined X-ray and EUV irradiation, with the magenta contour indicating the point at which the flow develops a significant neutral fraction and beyond which the EUV cannot penetrate. This is easily understand if we consider the Strömgen radius:

$$r_s \approx 0.2 \text{ AU} \left(\frac{\Phi_*}{10^{41} \text{ s}^{-1}} \right)^{1/3} \left(\frac{n}{10^8 \text{ cm}^{-3}} \right)^{-2/3} \quad (10)$$

where $n = 10^8 \text{ cm}^{-3}$ is the density at the base of the flow for an X-ray luminosity of $L_X = 2 \times 10^{30} \text{ erg s}^{-1}$. Now, Equation 7 (or Appendix A) implies the density scales linearly with X-ray luminosity ($n \propto L_X$). If we furthermore assume that the EUV and X-ray luminosity are both coronally produced (e.g. Alexander et al. 2005), so the luminosities scale linearly we find $r_s \propto L_X^{-1/3}$. This means that even at the lowest X-ray luminosities ($\sim 10^{28} \text{ erg s}^{-1}$) the EUV penetration is still too small to penetrate the X-ray flow. Even if we adopt the strongest EUV and the weakest X-ray luminosities quoted in the literature (i.e. $L_X = 10^{28} \text{ erg s}^{-1}$, $\Phi_* = 10^{44} \text{ s}^{-1}$; Güdel et al. 2007; Alexander et al. 2005) we find that the EUV flux cannot reach the surface of the disc from which the bulk of the X-ray wind is launched. Therefore, EUV irradiation can be neglected when X-ray radiation is also present.

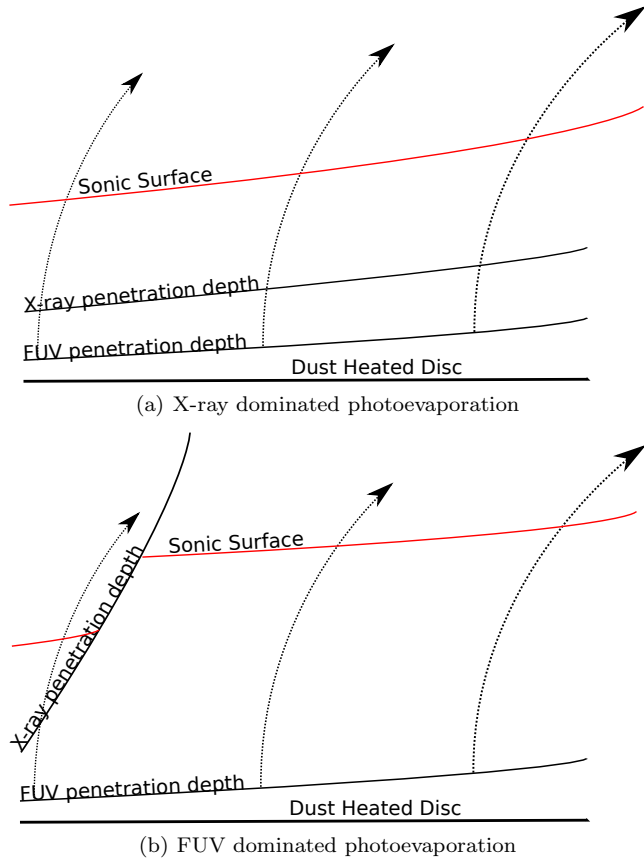


Figure 3. Figure showing a cartoon sketch of photoevaporation from a disc exposed to UV and X-ray irradiation. The flow begins in the FUV heated region, but at some height the flow transitions to the X-ray heated region and then passes through the sonic surface in the X-ray heated region.

3.2 FUV and X-ray heated flows

Gorti & Hollenbach (2008,2009) considered the combined effect of UV and X-ray heating in setting the hydrostatic disc structure and then used their static structures to predict resulting flow rates. In the case of FUV heating, the underlying heated disc structure determines the properties at the sonic surface and a variety of solutions, whether static or flowing, asymptote to the same (nearly hydrostatic) structure at small z . Although the results of Gorti & Hollenbach still represent the state of the art in terms of the thermal and chemical structure of X-ray and FUV irradiated discs, the implications of these studies for the resulting mass loss rate are currently unclear. In Section 5 we explore this further by using a simple parametrisation of FUV heating in our radiation hydrodynamical simulations (although we caution this should not be regarded as a proper treatment of the FUV heated flow). Here we discuss the general theoretical framework for combined FUV and X-ray heated flows.

X-ray heating is effective up to a total hydrogen column of around 10^{22} cm^{-2} . For models using depleted dust in the disc atmosphere (as in the models of D’Alessio et al. 1998,1999,2001), FUV heating extends to significantly higher columns. This means that travelling along a line from the star to a point in the disc one first traverses gas that is

exposed to both X-rays⁵ and FUV, then to FUV only and then to neither. Within ~ 100 AU the X-rays dominate the heating in the regions that are exposed to both X-rays and FUV. Therefore, in this region the sequence (as one proceeds away from the star) is X-ray heated, FUV heated and then heated by neither - in reality heated by coupling to the dust - (e.g. Gorti & Hollenbach, 2009).

Though we expect this sequence of X-ray heating followed by FUV heating, there are still two topologically distinct possibilities which we illustrate⁶ in Figure 3. Figure 3(a) is a schematic illustration of the case where the flow in the FUV heated region never exceeds its local sound speed for any of the streamlines shown. The sonic transition occurs in the X-ray heated region. In this case we can use the previous arguments to find that the sound speed at the X-ray heated sonic surface is simply given by Equation 4 to order unity as before: in other words the temperature at the sonic surface is simply a function of cylindrical radius. Since this also fixes the density at the sonic surface this implies that the mass flux is just a function of R and X-ray luminosity. In other words, whatever the detailed physics of the heating and cooling processes in the X-ray dark region, they must combine to drive a flow that is able to deliver the required mass flux to the X-ray sonic surface. We therefore expect that if the geometry is as shown in Figure 3(a), the photoevaporation rate is entirely controlled by X-ray heating.

On the other hand, Figure 3(b) shows three streamlines where the two at larger radius undergo a sonic transition within the FUV heated region. In this case the flow has to self-adjust to deliver the required conditions at the FUV sonic surface - in other words it is the structure of the FUV heated region that controls the mass flow rate. Although in principle gas flowing out in this FUV heated wind could become X-ray heated at some point, this region would not be causally connected to the flow base, the two regions being separated by a shock. However, it is unlikely that an FUV driven wind would ever be significantly heated by X-rays from the central star. This is because we require the condition at the sonic surface in the FUV heated region to satisfy Equation 4. Given that FUV heating does not generally attain temperatures in excess of $\sim 1000 - 2000\text{K}$ (Gorti & Hollenbach 2004; Bruderer et al. 2009), this implies that the schematic FUV sonic surface shown in Figure 3(b) must lie at radii of ≥ 100 AU where X-rays are incapable of heating the gas to greater temperatures than the FUV.

We therefore conclude that FUV driven winds are only likely to be significant at radii > 100 AU. If the flow topology at smaller radii is as shown in Figure 3(a) then the photoevaporation rate is set entirely by the X-rays. The only situation in which FUV heating could control mass loss from much smaller radii is if the streamlines crossing the FUV sonic surface at > 100 AU actually originated

⁵ By X-rays we are referring to the X-ray photons that provide significant thermal heating with a maximum energy of 1-2KeV and not those at higher energies that can penetrate larger columns but provide insignificant heating (see Ercolano et al. 2009b).

⁶ Note the similarity of this discussion to the analysis of flow from protoplanetary discs in the case of combined irradiation by FUV and EUV radiation fields: see Johnstone et al 1998

at small radii. Naturally, we need to perform a radiation-hydrodynamic simulation with FUV heating to assess this possibility (Section 6).

4 NUMERICAL MODELS OF PHOTOEVAPORATING DISCS

As discussed in Section 2.3, numerical radiation-hydrodynamic simulations are required to obtain accurate mass-loss rates and importantly the mass-loss profile. In this section we extend the parameter space investigations by Owen et al. (2010, 2011b) to cover the entire range of X-ray luminosity, mass & inner hole size expected for discs around low-mass stars, and thus test and calibrate the theory discussed above. Owen et al. (2011b) already investigated the explicit dependence of mass-loss rate on X-ray luminosity and inner-hole size around a $0.7M_{\odot}$ star. Therefore, in this work we are only concerned with extending the models to lower mass and varying disc structures, and we have performed simulations of photoevaporating discs around 0.1 & $0.7 M_{\odot}$ star.

4.1 Numerical Method

The numerical method is similar to that described in Owen et al. (2010), and is briefly described here for completeness. The simulations were performed using a modified version of the ZEUS-MP/2 code⁷ (Hayes et al. 2006), where the modifications are described in detail in Owen et al. (2010). X-ray heating is included using a temperature-ionization parameter relation up-to a critical column of $N = 10^{22} \text{cm}^{-2}$; at columns larger than this value the gas temperature is fixed to the dust temperature. We start from the hydrostatic disc calculations of D’Alessio et al. (2001) that only include dust heating; this disc structure is then irradiated with X-rays which drive a photoevaporative wind that evolves to steady state. We also use spherical co-ordinates in order to match the symmetry of the solution at large radius.

4.1.1 Primordial Discs

In order to test the mass-scaling, along with the predicted X-ray luminosity scaling in different mass regimes, we perform 5 simulations of photoevaporation for a primordial disc around a $0.1M_{\odot}$ star, evenly spaced in logarithmic X-ray luminosity from $\log_{10} L_X = 28.3$ to 30.3 , which covers the range of observed X-ray luminosities around M-type stars. We use a grid with 288 logarithmically spaced cells in the radial direction and 144 cell equally spaced in the angular direction. The grid extends from $r = 0.03 \text{AU}$ ($\sim 0.03R_g$) to $r = 46 \text{AU}$ ($\geq 45R_g$) and thus covers the range where we expect photoevaporation to be important.

In order to consider the effect of varying the disc structure we run three further simulations of the original calculation performed in Owen et al. (2010), i.e. a disc around a $0.7M_{\odot}$ star with an X-ray luminosity of $2 \times 10^{30} \text{erg s}^{-1}$:

⁷ Note: In order to increase computational efficiency we have moved from the scalar ZEUS-2D code to the MPI ZEUS-MP/2, which parallelises efficiently on up-to 64 processors.

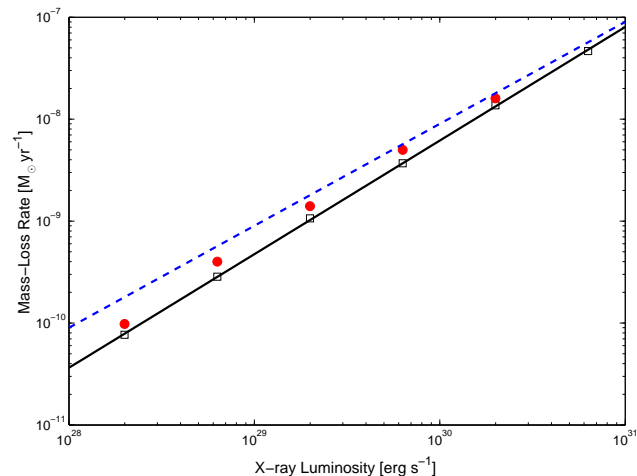


Figure 4. Mass-loss rate plotted against X-ray luminosity, the open squares show the simulations results for a $0.7M_{\odot}$ star obtained in Owen et al. (2011b), the filled circles show the simulation results for a $0.1M_{\odot}$ star described in this work. The solid line shows the fit to the mass-loss rates used for a population-synthesis study conducted in Owen et al. (2011b), the dashed line shows the order of magnitude estimate obtained in Section 3.

firstly we increase and decrease the dust temperature by a factor of $\sqrt{2}$, since the dust in the region that interacts with the X-ray heated region is optically thin. These changes in temperature effectively correspond to a change in the stellar luminosity by a factor of 4. We also consider a simulation with a disc mass of 10% of the original calculation i.e. $M_d = 2.6 \times 10^{-3} M_{\odot}$.

4.1.2 Discs with inner holes

Since the low stellar mass simulations presented here have lower disc masses than the higher mass counterparts described in Owen et al (2011b), we have to take into account of the fact that the density structure of the underlying disc may be being eroded during the hydrodynamical simulation on a time-scale less than the time required to set up a steady state wind (this latter being \sim the sound crossing time to the edge of the grid; see discussion in Alexander et al 2006a). Such erosion is not necessarily ‘realistic’ since we do not model the viscous effects in the disc which may re-supply material to the disc inner edge. In order to explore this effect we consider three classes of simulation: one with a small inner hole (0.7 AU) where the disc is not significantly depleted over the duration of the simulation, one starting with inner hole radius of 3 AU that was allowed to erode over the duration of the simulation and one with radius of 5 AU where the inner edge is ‘held’ at 5 AU by artificial re-supply (i.e by re-setting the X-ray dark ‘base density’ to its original value every time-step) to obtain a steady-state simulation. For each of these cases we model two X-ray luminosities ($\log L_X = 29.3, 30.3$).

4.2 Simulation results: primordial discs

In Figure 4 we show how the mass-loss rate scales with both mass and X-ray luminosity; the results confirm the theoretic-

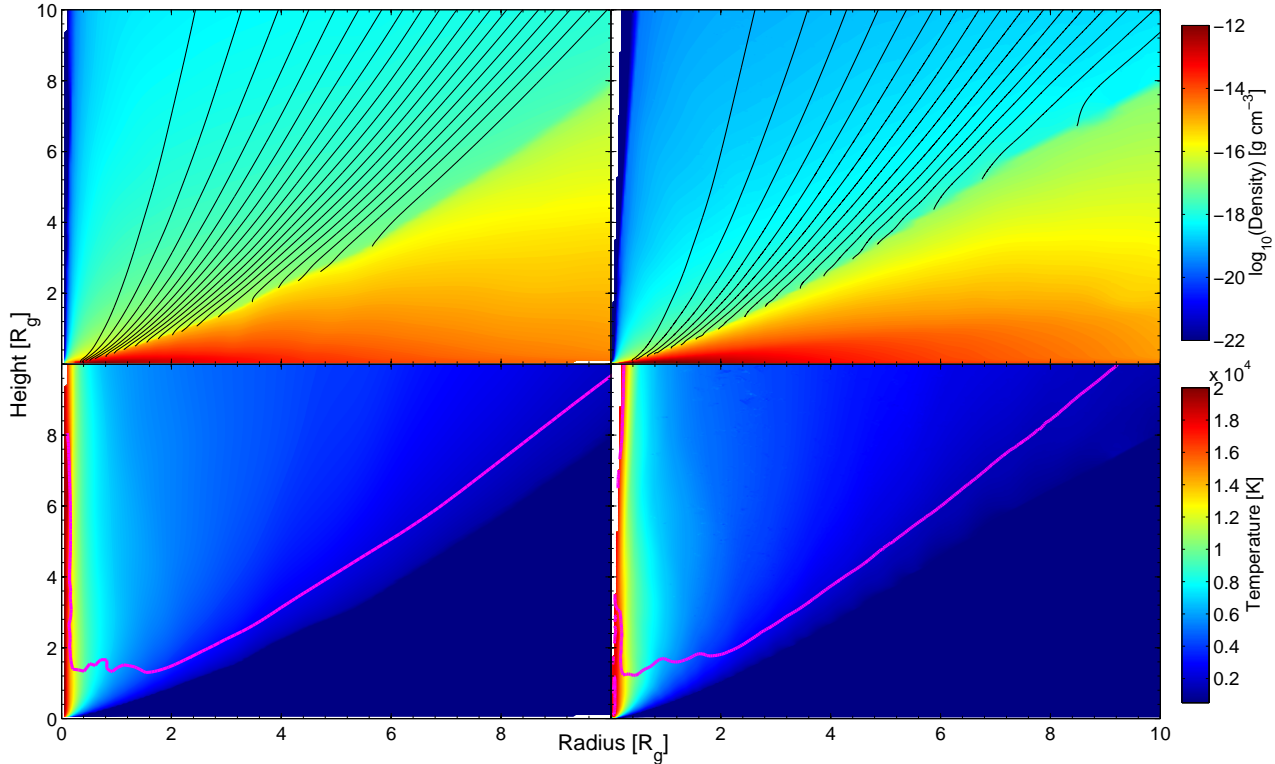


Figure 5. Figure showing the flow topology around a 0.1 (left panels) and 0.7 (right panels) M_{\odot} star for X-ray luminosity of $2 \times 10^{29} \text{ erg s}^{-1}$ and $2 \times 10^{30} \text{ erg s}^{-1}$ respectively; the results for the $0.7M_{\odot}$ star are taken from Owen et al. (2011b). The top panels show the density structure with streamlines at 5% intervals of the cumulative mass-loss rate. The lower panels show the temperature structure of the flow, where the solid line represents the sonic surface. We note (in agreement with the theoretical model presented in Section 2) that the mass-loss profile and temperature are independent of stellar mass when considered in terms of a radius scaled by r_g , but the density structure scales as M_{*}^{-2} .

cal predictions described in Section 2.2 to first order, namely no explicit mass-dependence on the photoevaporation rate and furthermore a mass-loss rate that scales approximately linearly with X-ray luminosity.

In Figure 5 we compare the flow morphology for an X-ray luminosity of $2 \times 10^{29} \text{ erg s}^{-1}$ around the 0.1 (left panels) and $0.7M_{\odot}$ (right panels) stars. The possible existence of self-similarity described in Appendix A implies that the temperature of the flow should be fixed by the value of the effective potential, thus to first order the temperature in the flow should be fixed by the mass of the central star and thus be scale free when considered in terms of a radius scaled by r_g . The lower panels of Figure 5 show that to first order this is the case. Furthermore the top panels show the density structure in the flow and the streamlines at 5% intervals of the cumulative mass loss rate. Despite small differences the similarity of the right and left hand panels demonstrate that the simulations are close to being self-similar. Moreover, the density is lower at the higher mass (at given R/R_g) by a factor consistent with the M_{*}^{-2} scaling predicted in Section 2 and Appendix A. We thus find that the simulations are in good agreement with the self-similarity arguments presented in Appendix A.

4.2.1 Dependence on disc structure

As first indicated by the numerical models calculated in Owen et al. (2010) with adiabatic discs, the disc structure has very little bearing on the final mass-loss rate. In Section 2 we developed an argument to explain this insensitivity to underlying disc structure, invoking the necessity to satisfy particular conditions on the X-ray sonic surface. Here we test this idea further by exploring the winds produced by more realistic variations in disc structure.

These correspond to variations in the stellar luminosity and underlying disc mass. Given the theoretical description of the flow predicts that the sonic surface controls the mass-flux, in Figure 6 we show the temperature at the sonic surface as a function of cylindrical radius. The black line shows the escape temperature as a function of radius. We see that beyond $\sim R_g$ the models are close to the escape temperature, in line with the expectation of Equation 4. At smaller radii, the escape temperature rises more steeply with decreasing radius than the models. We can simply understand this change in behaviour by noting that it occurs at a temperature of around 10^4 K , which is where the ionisation parameter temperature relation flattens (see Figure 1). At higher temperatures the temperature is rather insensitive to ionisation parameter. Thus, whereas at larger radius, the ionisation parameter adjusts to produce the temperature at the sonic surface demanded by Equation 4, at small ra-

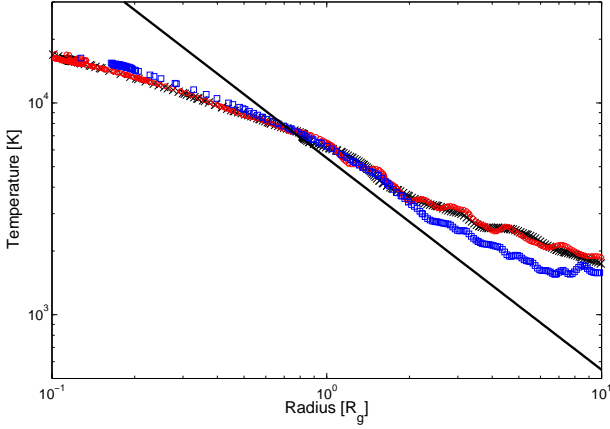


Figure 6. The temperature at the sonic surface as a function of cylindrical radii (scaled by R_g) for 3 models with two different stellar masses (0.1 & $0.7M_\odot$) and X-ray luminosities of (2×10^{29} & $2 \times 10^{30} \text{ erg s}^{-1}$). The open squares show the original $0.7M_\odot$, $2 \times 10^{30} \text{ erg s}^{-1}$ calculated by Owen et al. (2010), the black crosses are those of the $0.1M_\odot$, $2 \times 10^{29} \text{ erg s}^{-1}$ and the open circles are for the $0.7M_\odot$, $2 \times 10^{30} \text{ erg s}^{-1}$ model calculated with at disc depleted in mass by a factor of 10 from the original calculation. The black line shows the temperature expected from the order of magnitude calculations performed in Section 2. We note all primordial disc calculations have sonic temperatures that follow similar loci.

dius the temperature is more or less fixed. In this case, the Parker wind sonic transition corresponds to an almost constant spherical radius. This transition can be seen in the topology of the sonic surface at $R \sim R_g$ in Figures 5 & 8. We further demonstrate this behaviour in Figure 7 which plots, for a variety of models, the effective potential on the sonic surface as a function of cylindrical radius - evidently all models evolve so as to satisfy a common relation on the sonic surface, regardless of the mass and temperature of the underlying disc.

Figure 8 illustrates the flow topology for the models with various disc temperatures and disc mass. Evidently these are qualitatively similar but differ in detail. For example, the sonic surface is at lower height and the density at intermediate height above the disc plane is reduced when the disc mass is lowered. This however has a minimal effect on the disc mass loss profiles: even a change in height of the sonic surface by 20 – 30% has a small effect on the effective potential on the sonic surface and hence hardly affects the associated temperature, density and mass flux. Figure 7 shows that for most radii the value of the effective potential is as expected. The dip at $R < 5\text{AU}$ represents the region described above that is unable to reach the required escape temperature and thus the sonic surface occurs at a constant height and the $z \gg R$ assumption breaks down. This can be understood in terms of the model described in Section 2: the sound speed at the sonic surface scales as $c_s^2 \sim \Psi_{\text{eff}} \sim GM_*/2R[2 - (z/R)^2]$, so that provided $z \gg R$, order unity variations in height correspond to small variations in the effective potential (see Figure 7). Thus the sound speed (and hence density and mass flux) at the sonic surface are insensitive to such changes in the height of the sonic surface. Since the mass-flux is predetermined then the sub-sonic flow structure adjusts itself to

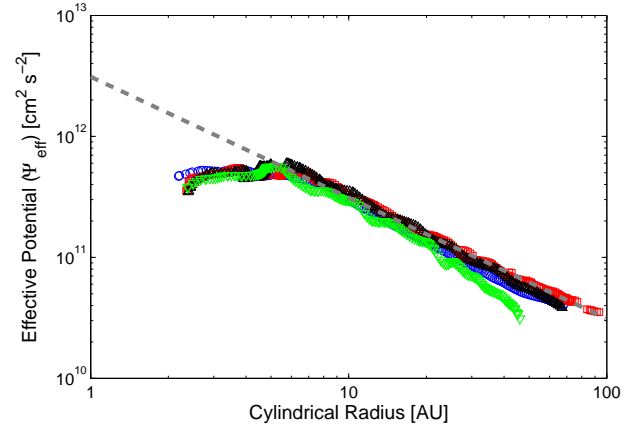


Figure 7. The value of the effective potential ($h^2/2R^2 - GM_*/r$ - note it is shown as a positive value for simplicity) at the sonic surface plotted against cylindrical radius for various underlying disc structures. The blue points are for the original calculation of Owen et al. 2010, the black points represents the mass depleted disc described above, the red points show the disc with increased dust temperature while the green points show the disc with decreased dust temperature as described above. The dashed line shows the prediction from the model described in Section 2.

feed the sonic surface at this required rate. This results in a flow topology that is fairly independent of the temperature or density in the disc, even though it is ultimately these quantities that determine the actual location of the sonic surface. As expected we find that the total mass-loss rates and profiles are fairly invariant to dramatic changes in disc structure: the total mass-loss rates for the modified discs range between $0.9 - 1.7 \times 10^{-8} M_\odot \text{ yr}^{-1}$ compared to the original $1.4 \times 10^{-8} M_\odot \text{ yr}^{-1}$ (Owen et al. 2010) for the same X-ray luminosity.

4.2.2 X-ray attenuation

The basic theoretical outline described in Section 2 assumed that the heating at the sonic surface is dominated by optically thin X-ray photons. In the numerical models we also adopt an optically thin X-ray heating model with a hard column cut-off at $N = 10^{22} \text{ cm}^{-2}$. In order to assess the consequences of these simplifications, we have performed additional simulations where the ionization parameter is instead given by:

$$\xi = \frac{L_X e^{-\tau}}{nr^2} \quad (11)$$

In the case of a monochromatic X-ray source, this would simply replace the X-ray flux with its value attenuated by the appropriate optical depth at that energy. However, in reality we have a broad range of energies, and it is less clear how to attenuate the flux - in practice the attenuation factor will reflect that for the photons that dominate the heating locally. Use of the ionisation parameter-temperature relation sidesteps the need to follow the propagation of photons of different energy and we thus do not have the information to model the attenuation properly. However, we can explore the consequences of attenuation by toy models in which the

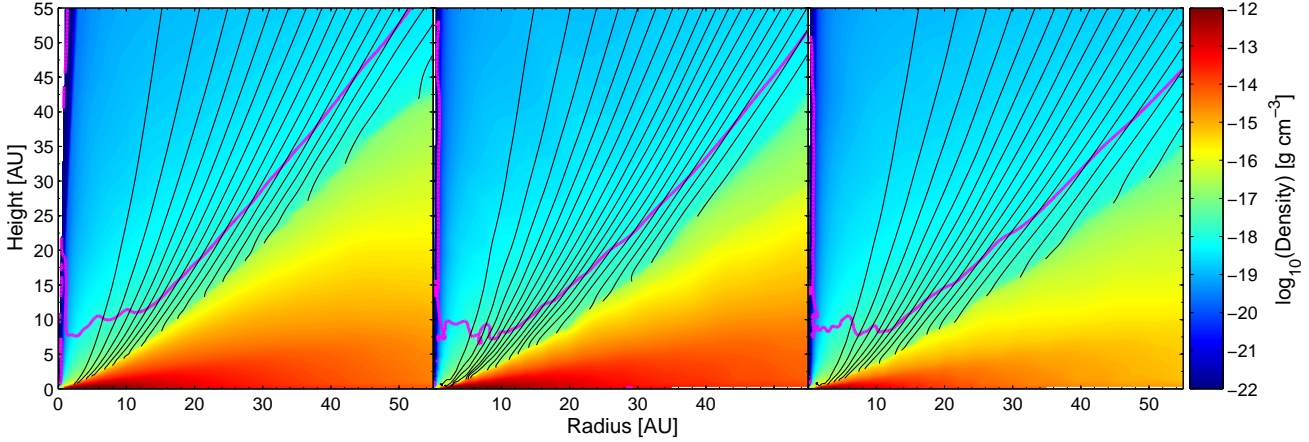


Figure 8. Density and velocity structure for photoevaporative winds with same stellar parameters ($M_* = 0.7M_\odot$, $L_X = 2 \times 10^{30}$ erg s^{-1}) but varying disc structures. From left to right: Original calculation by Owen et al. (2010); a reduction in dust temperature by $\sqrt{2}$; a reduction in the disc mass by a factor of 10. All figures shows very similar velocity and density structures in the wind.

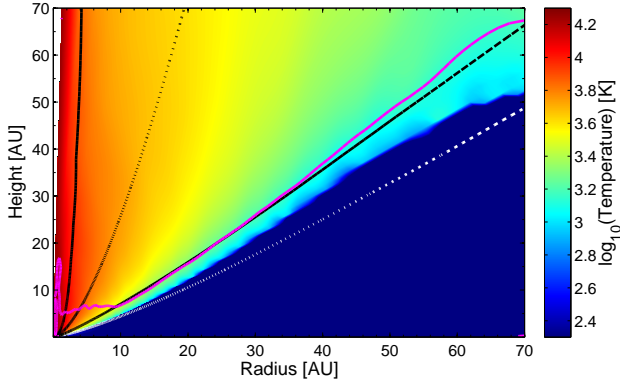


Figure 9. Temperature structure of the wind from a star with an X-ray luminosity of $L_X = 2 \times 10^{30}$ erg s^{-1} and a stellar mass $0.7M_\odot$. The solid magenta line shows the sonic surface, dot-dashed line a column of 10^{22} cm^{-2} , the dashed line a column of 10^{21} cm^{-2} , the dotted line a column of 10^{20} cm^{-2} and the solid black line a column of 10^{19} cm^{-2} . Cold regions at columns $< 10^{22}$ cm^{-2} indicate regions where the dust temperature is higher than the temperature given by X-ray heating.

optical depth of unity is fixed to three characteristic columns $N = 10^{20}$, 10^{21} , 10^{22} cm^{-2} . The models with X-rays attenuated at column densities of 10^{21} and 10^{22} cm^{-2} show little difference in structure and mass-loss rate to that performed by Owen et al. (2010). However, the model with attenuation at a column density of 10^{20} cm^{-2} is unable to heat the outer regions of the disc and the flow is restricted to the inner $R \leq 10$ AU, resulting in a significantly reduced mass-loss rate. We can understand this result by inspecting Figure 9, which superposes contours of equal column density to the source on a temperature map in the case of a model without attenuation. We see that the contour with a column to the star of 10^{21} cm^{-2} lies close to the sonic surface and thus (given the arguments that we have given here about the importance of the sonic surface in setting the mass flux) we expect that attenuation at column densities of 10^{21} cm^{-2} or above will not greatly affect the mass flow.

We now need to ask whether the extreme attenuation model (i.e. that with an attenuation column of 10^{20} cm^{-2} , which does suppress the mass-loss) is physically reasonable. Such an attenuation column would be appropriate to photons of energy ~ 0.1 keV. Thus to argue that 10^{20} cm^{-2} is the relevant column density is to argue that photons of higher energy (i.e. > 0.1 keV) are minor contributors to heating gas to the temperatures (3000 – 5000K) in the region of the sonic surface that dominates the mass-loss.

The most convincing argument that the higher energy photons ($\geq 0.3 - 0.4$ keV) are dominating the heating to temperatures ≤ 5000 K is provided by the exercise conducted in Owen et al. (2010). In this exercise, the wind structure of a high density ($L_X = 2 \times 10^{30}$ erg s^{-1}) unattenuated steady state wind (obtained from a hydrodynamic calculation using an ionization parameter approach) was fed in to the MOCASSIN Monte Carlo radiative transfer code (Ercolano et al. 2003,2005,2008), which self-consistently follows the attenuation and propagation of X-ray photon packets as a function of energy. The results of this exercise, shown in Figure 9 of Owen et al. (2010), confirmed that the agreement between the parametrised temperatures used in the hydrodynamics and the temperatures generated by MOCASSIN is excellent. We infer from this that it is higher energy photons ($\geq 0.3 - 0.4$ keV) that are mainly responsible for heating the region of the sonic surface that dominates the mass-flux to the required temperatures (≤ 5000 K).

4.3 Simulation Results: inner hole discs

In Figure 10 we show the mass-loss rates as a function of inner-hole size for the low mass stars ($0.1M_\odot$) compared with previous results of the higher mass-stars.

As in the simulations reported in Owen et al. (2011b) we find that the mass-loss rate is approximately independent of the inner hole size. Figure 10 also shows that the steady-state simulations (squares) give identical results to the eroding simulations, giving confidence that the mass-loss rates obtained from the eroding simulations are accurate over the range of radii considered. The simulations show as expected that the mass-loss rate scaling is also linear with X-

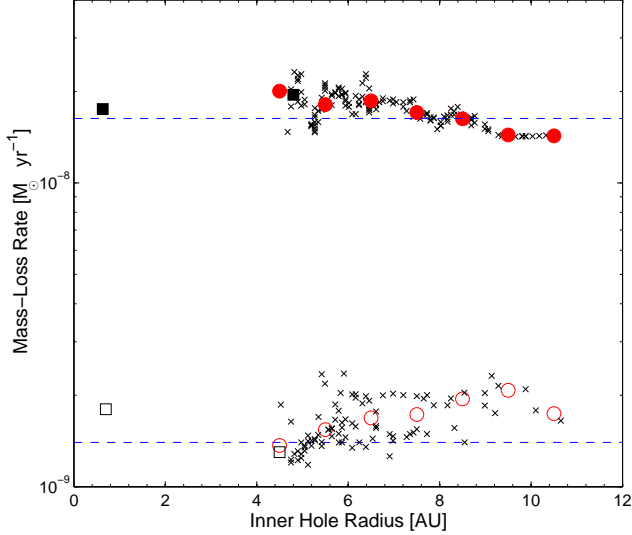


Figure 10. Figure showing the mass-loss rate as a function of inner hole size for discs around a $0.1M_{\odot}$ star. The filled points are those for an X-ray luminosity of $2 \times 10^{30} \text{ erg s}^{-1}$ and the open points are those for an X-ray luminosity of $2 \times 10^{29} \text{ erg s}^{-1}$. The crosses are the mass-loss rates calculated from the eroded inner hole models, while the circles are the moving average calculated from these eroding mass-loss rates and the squares are the mass-loss rates from simulations which are maintained in steady-state. The dashed line shows the mass-loss rates for primordial discs with the same X-ray luminosity.

ray luminosity in agreement with the theoretical arguments presented in Section 2 and with previous simulations.

4.3.1 Understanding the Inner hole Scalings

Examination of the streamline topology for various inner hole radii (over a factor of ~ 2) suggests that the topology of the innermost streamline is approximately scale free (i.e. with an over all radial scale that varies with R_{hole}); in consequence the variation of temperature and velocity along this streamline (as a function of distance along the streamline scaled to R_{hole}) is approximately the same in each simulation (see Figure 11). This encourages us to construct a scaling argument even though in the Appendix we show models with different R_{hole} cannot be exactly self-similar. There is no *a priori* reason one would expect the temperature structure of these flows to be identical: this only follows if we use the numerical result that the streamline topology is fixed. We argue in the Appendix that the fact that the relationship between the ionization parameter and temperature is not a simple power law implies that the conditions along two topologically identical streamlines can only be scaled to each other if the variation of temperature with (scaled) distance along the streamline is the same in both cases. Then the mass-flux scales as $n(l)A(l)$. For fixed temperature Equation 7 implies $n \propto R_{\text{hole}}^{-2}$ and the stream-bundle area scales as $A \propto R_{\text{hole}}^2$. Therefore, along this streamline the mass-flux is fixed and does not scale with inner hole radius.

The origin of a scalable innermost streamline is likely to originate from the fact that unlike primordial discs (where the thermal pressure is dominant in determining the stream-

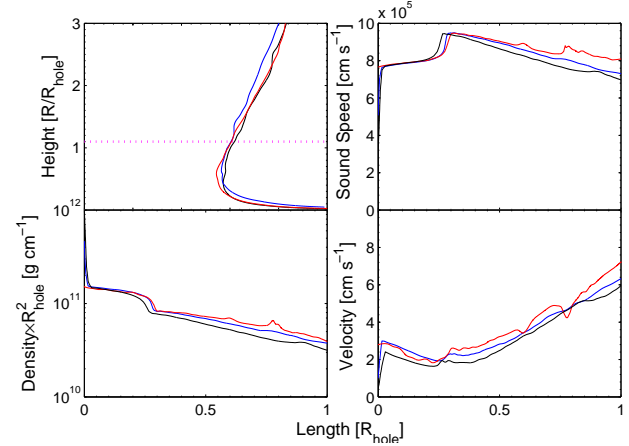


Figure 11. Figure showing the streamline topology and density, sound speed and velocity along the sub-sonic section of the streamline. The streamline topology is shown in the top left hand panel scaled in terms of R_{hole} , with the sonic surface shown as the dotted line. Then bottom left panel show the density $\times R_{\text{hole}}^2$, the top right show the sound speed and the bottom right show the velocity as a function of distance along the streamline normalised to R_{hole} . The black lines are for a hole of 14 AU, the blue line for a hole of 21AU and the red for an inner hole of 30 AU.

line), in this case the centrifugal force is important since material that is stripped from the rim of an inner hole initially moves inwards. As the effective potential is scalable in terms of R_{hole} then it follows that (in the limit of negligible pressure) the streamline topology would also be scalable in terms of R_{hole} . Provided the total mass-flux is dominated from the inner hole region - as the simulations indicate - then the total mass-loss should scale in a similar fashion to the mass-flux on the innermost stream-bundle, resulting in a total mass-loss rate that is approximately independent of the inner hole radius.

5 NUMERICAL TESTS: INCLUDING ‘FUV-TYPE’ HEATING

In Section 3 we argued that at radii $< 100 \text{ AU}$ the flow morphology is likely to resemble that shown in Figure 3(a) where the mass loss rate is set entirely by the conditions at the X-ray sonic surfaces and where any FUV heating deeper must produce a flow that self-adjusts to supply the correct mass flux at the X-ray sonic surface. In order to test whether the flow topology resembles that shown in Figure 3(a) we perform some simulations that roughly aim to include the effect of extra-heating below the X-ray dominated region. If FUV heating was important to the calculation of photoevaporation rates then one would require a detailed calculation of X-ray and FUV heating and cooling, along the lines of combining the X-ray algorithm with an FUV algorithm (e.g. Richling & Yorke, 2000). While such a calculation would be necessary to predict line emission from the warm atomic and molecular layer, we are here interested in the simpler question of whether a plausible modification of the structure at the base of the flow due to the effect of FUV heating will influence the flow at the X-ray sonic surface. Therefore, a full X-ray +UV calculation is unnecessary and beyond the scope

of this work and we instead employ a simple prescription for FUV heating at the base of the flow.

We calculate the FUV flux throughout the disc/wind system in an identical manner to Richling & Yorke (2000), including opacity only from dust extinction (e.g. we ignore opacity arising from the ionization of Carbon and Sulphur, thus overestimating the flux and gas temperature). We then turn the attenuated FUV flux into a temperature using a parametrisation of the previous FUV calculations of Richling & Yorke (2000) and FUV heating calculation of Gorti & Hollenbach (2008):

$$T_{\text{FUV}} = 1400\text{K} \left(\frac{f_{\text{FUV}}}{300 \text{ erg s}^{-1} \text{ cm}^{-2}} \right)^{0.35} \left(\frac{n}{5 \times 10^6 \text{ cm}^{-3}} \right)^{-0.25} \quad (12)$$

where f_{FUV} is the attenuated FUV flux. This parametrisation reproduces the temperature structure of the region directly irradiated by FUV in Richling & Yorke (2000) (their model A) and the temperature structure listed for the ‘launching point’ of the calculations of Gorti & Hollenbach (2008). We perform three simulation with a large FUV luminosity of $1 \times 10^{31} \text{ erg s}^{-1}$ where we vary the FUV extinction, and choose a depleted (from ISM type dust) value of the FUV extinction of $300 \text{ cm}^2 \text{ g}^{-1}$ used by Richling & Yorke (2000) and a extinction that is depleted by a further factor of 10 to $30 \text{ cm}^2 \text{ g}^{-1}$. Furthermore the calculations of Gorti et al. (2009) indicate that more depleted discs drive more efficient flows (as in their calculations the mass-loss remains constant as the accretion rate - and thus FUV luminosity - falls). Therefore, we perform a calculation using the low mass disc described earlier ($M_d = 2.6 \times 10^{-3} M_{\odot}$) and use an FUV extinction of $2 \text{ cm}^2 \text{ g}^{-1}$ indicative of a very heavily settled disc atmosphere (D’Alessio et al. 1998,1999). At every point in the disc/wind system we choose the heating mechanism (X-rays, FUV or dust) that produces the highest temperature, where we note the dust temperatures used already include the effects of FUV heating from accretion luminosity as well as the chromospheric contribution (D’alessio et al. 2001). Furthermore, as we attenuate the FUV flux there is no need to apply a column cut-off as in the X-ray case. Thus provided the FUV gas temperature is higher than the X-ray or dust temperature at any point in the grid (even those with $N_H > 10^{22} \text{ cm}^{-2}$) it can be heated by the FUV radiation. The FUV extinction is fixed throughout the calculation domain: this is reasonably valid as Owen et al. (2011a) showed that photoevaporative winds are capable of entraining small dust particles, which will dominate the opacity at FUV wavelengths. We emphasise that this is no attempt to calculate the self-consistent thermal structure of a disc heated by FUV/X-rays, but purely an investigation into the influence of FUV type heating at the base of an X-ray heated flow. We demonstrate this further by running calculations in which we vary the parametrisation; while this of course has no physical basis it is purely a simple way to demonstrate that are our results are not being driven by our detailed assumptions about FUV heating. We thus calculate an extra 4 models for the maximum FUV penetration model, where we vary the power law indices (in Equation 12 in all four possible combinations) of the flux and density variation by factors two in both directions.

Finally, we investigate whether the X-ray to FUV luminosity ratio has any bearing on the results (particularly

any transition from the flow topology shown in Figure 3(a) to Figure 3(b) when the X-rays are weak compared to the FUV luminosity). We thus fix the FUV luminosity at the large value of $1 \times 10^{31} \text{ erg s}^{-1}$ and systematically lower the X-ray luminosity to the lowest values observed $\sim 10^{28} \text{ erg s}^{-1}$.

5.1 Results

Our calculations using this extra ‘FUV-type’ heating does not affect the mass-loss rates obtained (for $L_X = 2 \times 10^{30}$, $L_{\text{FUV}} = 1 \times 10^{31} \text{ erg s}^{-1}$): we find a value of $1.2 \times 10^{-8} M_{\odot} \text{ yr}^{-1}$ for the initial calculation with the same depleted FUV extinction coefficient as Richling & Yorke (2000), a value of $1.1 \times 10^{-8} M_{\odot} \text{ yr}^{-1}$ for the calculations with the very depleted FUV extinction coefficient, and a value of $1.3 \times 10^{-8} M_{\odot} \text{ yr}^{-1}$ for the mass depleted disc. In all simulations we find as expected that the sonic surface occurs in the X-ray heated regions and we therefore confirm the simple ideas presented in Section 2, as well as demonstrating that the photoevaporation rates are controlled by the X-ray physics alone.

In Figure 12 we show the density and velocity structure of the maximum FUV penetration model (i.e. the mass depleted disc). This shows as expected that the sonic surface occurs in the X-ray heating region, while the FUV heated flow is confined to a layer between the bound dust heated disc and the X-ray heated flow (i.e. between the two black lines in Figure 12). We further find that even though the density and temperature structure of the ‘FUV’ heated region varies between model runs, in all cases the thermal structure of the sonic surface is as shown in Figure 6. Therefore, the FUV layer must be adjusting its structure in order to ‘feed’ the X-ray heated region with the correct mass-flux, and satisfy the hydrodynamical conditions at the sonic surface. Therefore, extra heating below the X-ray heated region has little effect on the photoevaporation rates in the range $R \sim 1 - 100 \text{ AU}$.

The structure of the system shown above does allow in principle for some additional mass loss due to FUV heating if some of the gas between the two black lines flows radially outwards through the FUV heated wedge rather than feeding material to the X-ray sonic surface. If such a ‘wedge flow’ (see schematic depiction in Figure 13) did exist then (given the temperature of the FUV heated gas) it would not undergo a sonic transition until a radius of order 100 AU, i.e. close to the outer boundary of the grid. We find that gas does leave the grid sub-sonically in the FUV heated region. However, due to the use of outflow boundary conditions on this grid boundary, it is impossible to tell if this flow is real or an artefact of outflow boundary conditions (which are only exact for super-sonic flow). Therefore, we are unable to further hypothesise on the possible existence of such FUV ‘wedge’ flows.

5.1.1 Effect of X-ray luminosity

In Figure 14 we show how the mass-loss rates vary with decreasing X-ray luminosity, compared to the mass-loss rates expected from pure X-ray models. For $L_X > 10^{29} \text{ erg s}^{-1}$ the flow resembles that of Figure 12: the X-ray sonic surface

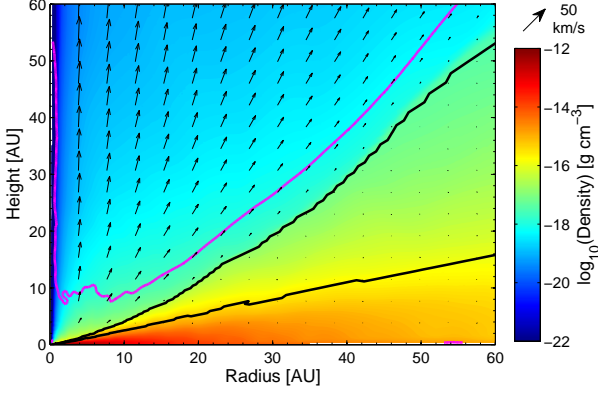


Figure 12. Velocity and Density structures of winds including an extra ‘FUV’ like heating mechanism, the arrows show the velocity in the wind and the black lines show regions where the extra heating mechanism is dominating over the X-rays and dust and the magenta contour shows the sonic surface. The model shown is the depleted disc with the extremely low FUV extinction allowing for maximum penetration of the underlying disc.

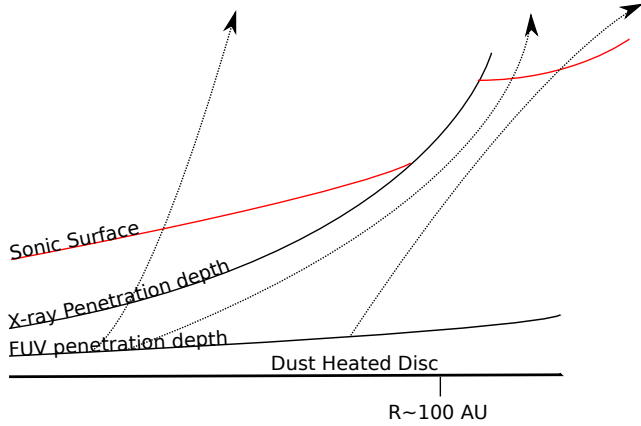


Figure 13. Cartoon of an X-ray flow with an FUV wedge flow underneath.

extends out to cylindrical radii ≥ 50 AU and sets the mass loss rate from the disc. At lower X-ray luminosities (for a fixed L_{FUV} of 10^{31} erg s^{-1}) the subsonic FUV region puffs up vertically and drives the X-ray sonic surface and upper region of the FUV heated region almost vertical at a radius of ~ 10 AU. This means that the predominant mass loss in the disc becomes at this point dominated by sub-sonic flow from the FUV region. As noted above, we do not trust the mass loss rates that we obtain in the case that material leaves the grid sub-sonically so that the mass loss rates at the low L_X end of Figure 14 should not be taken as a good measure of the total mass-loss rates. Thus considerably more investigation is required to describe photoevaporation in the limit of low X-ray to FUV luminosity ratios.

Instead, the chief result of Figure 14 is that the flow morphology and mass-loss rates are X-ray dominated provided that $L_X/L_{\text{FUV}} \geq 0.01$. While stars with X-ray luminosities $< 10^{29}$ erg s^{-1} only represent a small fraction $\sim 5 - 10\%$ of the population of young stars (Güedel et al. 2007; Owen et al. 2011b), the role of combined FUV/X-ray heated flows will certainly be important for these objects if

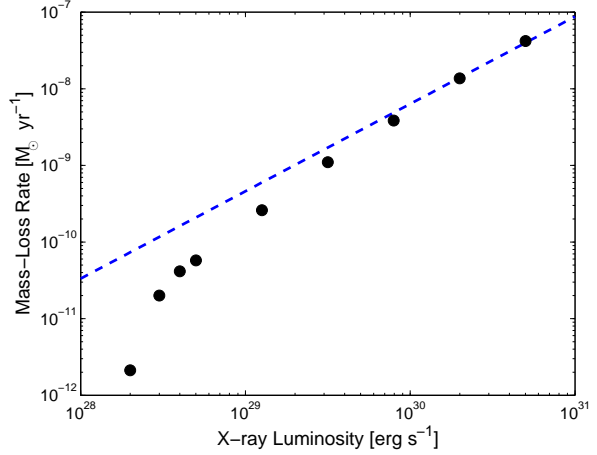


Figure 14. Mass-loss rates arising in the X-ray heated flow from models that include the FUV heating parametrisation, plotted as a function of X-ray luminosity. The dotted line indicated the mass-loss rate expected from a pure X-ray model. See text for a discussion of the reliability of the results in the limit of low X-ray luminosities.

the FUV luminosity continues to remain large ($\sim 100L_X$) throughout the disc’s lifetime.

6 FINAL CLEARING OF THE DISC

In Figure 15 we show the evolution of a simulation with $M_* = 0.1M_\odot$ & $L_X = 2 \times 10^{30}$ erg s^{-1} in which the disc hole is eroded during the course of the simulation (and for which the mass-loss rate during the evolution is shown by the crosses in Figure 10). During the first 300 years of evolution, the photoevaporative flow slowly strips off gas from the inner edge of the disc. During this stage, there is a *radially thin* layer of bound X-ray heated gas ($T_X \sim 200 - 400\text{K}$) on the inside rim of the disc and the flow direction of the escaping gas is radially *inwards*. The origin of this layer is fairly easy to understand: as the fixed streamline topology suggested by the simulations fixes the density and structure in the flow, the flow cannot by construction consist of a fixed column density. It turns out that the column density of the flow is much less than 10^{22} cm^{-2} . Therefore, the X-ray heated region must contain not only the flow but also a warm bound X-ray heated region, that is separated from the flow by a contact discontinuity. As the hole grows, the radial width of the layer of warm bound X-ray heated gas grows in size in order to still maintain the critical column density for X-ray heating of 10^{22} cm^{-2} . Once the hole size grows to $R_{\text{hole}} \sim 10\text{AU}$, the radial width of this region becomes comparable with the vertical scale height of the X-ray heated gas. At this point, the topology of the X-ray heated gas just within the rim changes from nearly radial inflow to one where there is a strong (roughly sonic) expansion velocity *normal to the disc plane*. This is seen in Figure 15 as the plume at the inner edge of the outer disc which, in the lower panels, rolls over to envelope the disc. The importance of this change of flow topology is that it allows gas to be evacuated out of the line of sight between the X-ray source and the disc rim. This thus increases the penetration of X-rays in the mid-

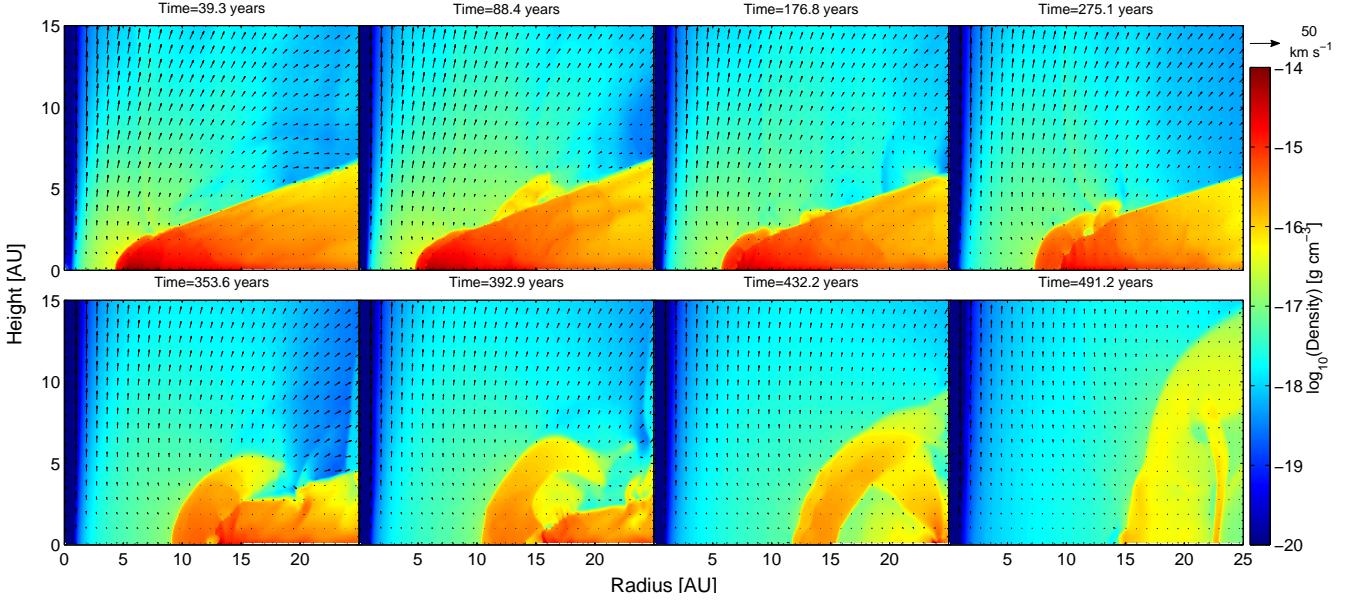


Figure 15. Time evolution of a simulation of a disc with an eroding inner hole and an X-ray luminosity of $2 \times 10^{30} \text{erg s}^{-1}$ around a $0.1M_{\odot}$ star. The colour map shows the density structure and the arrows indicate the velocity structure. Each panel indicates a snapshot of the flow structure.

plane. The panels at 353.6 years and 392. years illustrate the formation of a low density bubble of heated gas between the expanding plume and the residual disc. One can also discern that this bubble is expanding radially into the disc and compressing the disc’s inner rim. We term this effect ‘thermal sweeping’ and note that it operates on a roughly dynamical time-scale (i.e. ~ 100 years at 10AU) which is not much more than the free expansion time of X-ray heated gas. We emphasise that this evolution is much faster than what occurs in the early stages of clearing inner hole discs, when the erosion rate is limited by the fact that the flow is radial and hence the evaporating gas continues to provide a degree of shielding to the disc’s inner rim.

This ‘thermal sweeping’ was not seen in the simulations calculated in Owen et al. (2010,2011b) for discs around a $0.7M_{\odot}$ star. We can understand this difference in that our simulations have a constant initial disc to star mass ratio and the previous simulations therefore had higher disc masses and higher mid-plane densities. This implies that the critical column for X-ray absorption was attained over a correspondingly smaller radial length scale; thus, at a given radius, the ratio of radial thickness to vertical scale height of the X-ray heated gas is smaller in the simulations with higher disc mass. These simulations therefore remained in the regime where the stripped gas moved radially inwards; we expect that (if we had the computational resources to calculate inner hole models around higher mass stars with very large radii) we would at some stage have entered the regime where the heated layer became radially thick and that ‘thermal sweeping’ would ensue in this case also.

When this X-ray warm, bound region is small it must be in dynamical balance with the photoevaporative flow and the dust heated disc. The time-scale on which it can obtain this equilibrium is the sound crossing time of the region $t_{sc} \approx \Delta/c_s$, where Δ is the width of this region. When $\Delta/H \ll 1$ (where H is the vertical scale height), this re-

gion can adjust to dynamical equilibrium quickly and the disc/flow system is stable, even though the pressure in the region is significant. However, at the point when $\Delta \sim H$ this region cannot rapidly obtain dynamical equilibrium, and therefore will expand vertically on the same time-scale. This vertical expansion can clearly be seen in the time series plots, and as it expands the mid-plane density drops, resulting in higher temperatures. This in turn accelerates the vertical dispersal and a runaway ensues. Eventually, a high pressure region develops at the edge of the dust heated disc that pushes the remaining disc material away rapidly on the dynamical time-scale.

In order to model this process we use the fact that the warm bound X-ray heated region must be in dynamical equilibrium with both the photoevaporative flow and the dust heated disc. The pressure is largest where bound X-ray heated region meets the dust heated disc, this region is highly sub-sonic and the requirement of dynamical equilibrium is simply one of pressure equilibrium. Thus one may write:

$$k_B n_X T_X = P_{\text{dust}} \quad (13)$$

where n_X is the density of the bound X-ray heated region. Now we can use Equation 13 to find Δ :

$$\Delta = \frac{N_X}{n_X} \quad (14)$$

where N_X is the X-ray penetration depth (i.e. $N_X = 10^{22} \text{cm}^{-2}$). Thus the requirement for this process to begin $\Delta = H$, simply becomes:

$$P_{\text{dust}}(R) \leq \frac{N_X k_B T_X}{H(R)} \quad (15)$$

or :

$$\Sigma(R) \lesssim \sqrt{2\pi} \mu m_h N_X \sqrt{\frac{T_X}{T_{\text{dust}}}} \quad (16)$$

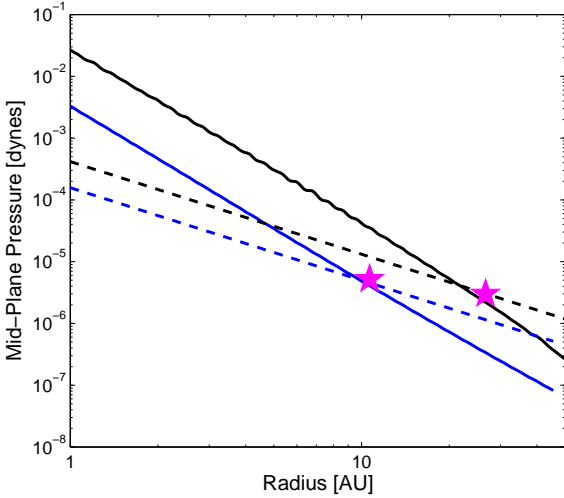


Figure 16. Plot of the LHS (solid- pressure of dust heated disc) and RHS (dashed-critical pressure of X-ray heated region) of Equation 15, to estimate the inner hole radii at which thermal sweeping begins. The stars show the radii the simulations indicate this process begins. Black represents a disc around a $0.7M_{\odot}$ star while blue shows a disc around a $0.1M_{\odot}$ (shown in Figure 15).

Substituting standard values into this equation we find:

$$\Sigma(R) \lesssim 0.43 \text{ g cm}^{-2} \left(\frac{\mu}{2.35} \right) \left(\frac{T_X}{400\text{K}} \right)^{1/2} \left(\frac{T_{\text{dust}}}{20\text{K}} \right)^{-1/2} \quad (17)$$

Thus this process will begin when the mid-plane pressure of the dust heated disc has dropped to a sufficiently small value, mainly through a reduction in the mid-plane density. This can be achieved either on account of a low disc mass or because the hole has grown to sufficiently large radius. This is shown in Figure 16 where in order to test the applicability of Equation 15 we also perform a re-simulation of model F from Owen et al. (2010) (a disc with an initial hole of 20 AU, an X-ray luminosity of $2 \times 10^{30} \text{ erg s}^{-1}$ and mass of $0.7M_{\odot}$), but the mid-plane pressure has been reduced to the point where Equation 15 predicts this process will occur when the disc hole size modestly exceeds its initial value. This re-simulation shows similar morphology to that shown in Figure 15 and the disc is completely cleared via the ‘thermal sweeping’ mechanism described above as the hole reaches $\sim 25 \text{ AU}$ (shown in black on Figure 16). The remaining disc mass just before this process sets in is around 5-10 Jupiter masses, and therefore a small fraction of the disc’s initial mass is cleared in this process: roughly $\sim 80\%$ of the disc’s initial material is accreted onto the star, $\sim 10\%$ lost in a photoevaporative wind and the final $\sim 10\%$ disperses through this process of ‘thermal sweeping’.

However, it is worth mentioning that these simulations were designed to study photoevaporative flows in the optically thin X-ray heated gas. On the other hand, once ‘thermal sweeping’ is initiated, the flow becomes sonic close to the location where X-ray heating is initiated and in this case a simple column cut-off will not accurately reproduce the thermal structure of this region. Furthermore, as the gas is considerably cooler (hundreds to thousands rather than thousands to tens of thousands K as in the photoevapora-

tion calculations) we cannot neglect the effect of molecular cooling, along with the added effect of FUV heating. This latter depends on the dust properties at the mid-plane of the disc at large radii: although the X-ray heated region is probably opaque to FUV radiation in the case of dust that is ISM-like, the FUV may penetrate beyond the X-ray heated region in the case of dust that is significantly depleted. The necessary calculations (including X-ray and FUV radiation along with dust evolution) are certainly beyond the scope of this work. We here restrict ourselves to stating that our simplified calculations suggest that the disc enters a ‘thermal sweeping’ phase (which clears the residual outer disc on roughly a dynamical time-scale) once the disc enters a region when the mid-plane pressure is sufficiently small.

Finally, while the instability sets in on dynamical time-scales, simple energetic calculations suggest it may take ~ 10 dynamical time-scales (at the inner edge) to unbind the outer regions of the disc at the lowest X-ray luminosities. This is somewhat longer than our simulations would predict in this case, since the simulations - by imposing radiative equilibrium - neglect the effect of adiabatic cooling. Hence, adiabatic cooling may be important during the final stages of ‘thermal sweeping’, but not during the initial stages (onset of the instability) as the amount of material contained in the bound X-ray heated region is small compared to the total disc mass. However, 10 dynamical time-scales (at the inner edge, $\sim 10^4$ years) is still considerably faster than any other gas removal process operating at this stage.

7 IMPLICATIONS FOR DISC EVOLUTION & DISPERSAL

The ultimate goal of the photoevaporation theory is to be able to predict disc evolution and lifetime based on properties of the underlying systems. At its most basic level we have shown throughout this work that it is only stellar X-ray luminosity that sets the photoevaporation rate and hence is the major factor in determining the disc lifetime. We have argued that the vigorous photoevaporation rates ($10^{-8} - 10^{-11} M_{\odot} \text{ yr}^{-1}$) are an inescapable consequence of X-ray irradiation (provided X-rays reach the disc’s surface, an issue discussed in detail in Section 8.2). Furthermore, we showed that variations in disc structure and the inclusion of EUV and FUV radiation fields have little effect on the flow structure and derived mass-loss rates provided $L_X/L_{\text{FUV}} > 0.01$.

The major consequence of this model is of course that discs around stars (of the same mass) with higher X-ray luminosities lose their discs first. An obvious implication of such a result is that disc-less stars will have on average a higher X-ray luminosity than disc-bearing stars at the same age. This has been observationally recognized for a while (e.g. Preibisch et al. 2005) and Owen et al. (2011b) showed that the X-ray photoevaporation model is quantitatively consistent with these observations. Ingleby et al. (2011) has attempted one of the first studies to investigate the role of high energy irradiation on disc dispersal; unfortunately the available X-ray data for the study was incomplete in both X-ray luminosity and mass, meaning it was impossible to disentangle the effects of stellar mass and X-ray luminosity on disc dispersal and the result was inconclusive. Now we

have fully developed the photoevaporation model down to lower masses, we would have been hopeful that it would be possible to make predictions of disc evolution as a function of stellar mass. However, as described in Section 8.1, the disc’s lifetime also depends on how the viscous time varies with stellar parameters and speculation about its variation with stellar mass is well beyond the aims of this paper. It is worth noting though that as discussed in Section 8.1, sensible assumptions lead to the conclusion that disc lifetime is not a strongly dependant function of stellar mass and is likely to decrease only weakly with increasing stellar mass, in agreement with the observations (e.g. Ercolano et al. 2011b).

7.1 Transition Discs

It was the observations of the frequency of ‘transition’ discs (Strom et al. 1989; Skrutskie et al. 1990; Kenyon & Hartman, 1995) that lead to the development of the photoevaporation mechanism. Since the original observations, the number of detected discs that are consistent with the original characteristics of a transition disc (i.e. a large drop in opacity at short wavelengths, while returning to primordial levels at longer wavelengths) has increased. However, there is no clear observational or theoretical consensus as to what a ‘transition’ disc actually is and it is becoming clear that the population of observed ‘transition’ discs are not a homogeneous sample (e.g. Alexander & Armitage, 2009; Owen et al. 2011b). The observations now span a range that includes accreting, non-accreting objects and those with small amounts of gas and dust inside the opacity ‘hole’; it is unlikely that one mechanism is responsible for all objects (Cieza et al. 2010). Some ‘transition’ disc samples are now being split into ‘transition’ and ‘pre-transition’ populations (e.g. Espaillat et al. 2010; Furlan et al. 2011).

The three main mechanisms that can account for the formation and structure of this class of objects are: photoevaporation, planet formation and grain growth. Owen et al. (2011b) showed that a large fraction ($\geq 50\%$) of solar type ‘transition’ discs were consistent with the X-ray photoevaporation scenario. In the X-ray photoevaporation scenario a ‘transition’ disc goes through two stages of evolution. Once the gap opens, the dust in the residual inner disc is rapidly (i.e on a time-scale much less than the viscous evolution time of the gas) depleted as a result of inward migration due to gas drag. The loss of dust (and its associated opacity) from the inner disc would result in the object being classified as a transition disc even while it still possesses an inner gas disc with its associated accretion. This phase lasts approximately $\sim 10\%$ of the observable disc’s lifetime. Once the inner disc has entirely drained onto the central star, the inner edge of the outer disc is directly exposed to X-ray irradiation and the outer disc is then eroded to large radius. During this phase a centrifugal barrier prevents material accreting from the inner-edge onto the star and the disc would appear as a non-accreting ‘transition’ disc with a large inner hole. The structural properties of observed ‘transition’/‘pre-transition’ disc are currently more detailed than the photoevaporation model can predict. This must await the development of coupled dust and gas evolution models that are correct when the dust-to-gas ratio is no longer small. Therefore, at this stage we do not distinguish between ‘transition’ and ‘pre-transition’ discs. Although discussed in Section 7.2 the in-

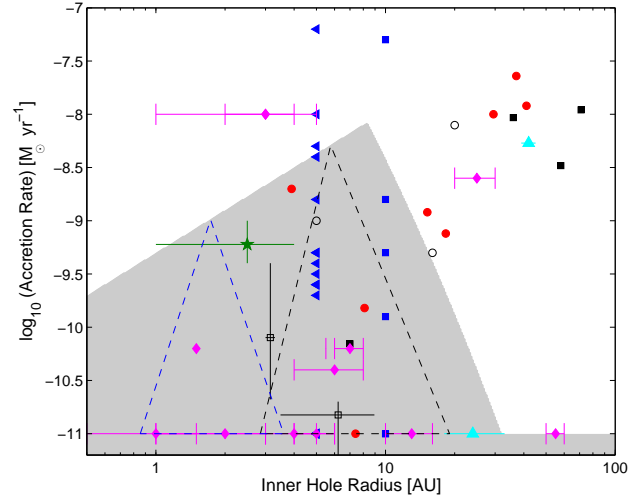


Figure 17. The inner hole radius and accretion rate of low-mass objects classified as ‘transition’ discs by various authors: cyan triangles (Brown et al. 2009); blue filled triangles & squares (Cieza et al. 2010); black open squares (Ercolano et al. 2009); black filled squares (Espaillat et al. 2008,2010); black open circles (Hughes et al. 2009, 2010); red filled circles (Kim et al. 2009); magenta filled diamonds (Merin et al. 2010); green filled star (Najita et al. 2010). Where error-bars or ranges are listed they are shown. Any object classified as non-accreting is placed on the plot with an accretion rate of $10^{-11}M_{\odot} \text{ yr}^{-1}$. The grey region represents the region of parameter space where the objects are consistent with gaps created by photoevaporation. See text for more details. The blue and black dashed regions represent those regions for a 0.3 and $1M_{\odot}$ star respectively.

clusion of ‘thermal sweeping’ significantly changes the accreting to non-accreting fraction predicted by previous photoevaporation models, to a population that will be a majority of accreting transition discs.

The observational data however also contains examples of transition discs with large inner holes ($R_{\text{hole}} \geq 20\text{AU}$) and large accretion rates ($\dot{M} \sim 10^{-8}M_{\odot} \text{ yr}^{-1}$) that are simply impossible to create through any kind of photoevaporation model. It has been suggested that these objects could have their large accretion rates set by FUV ionization and MRI activation at the inner edge of the hole (Perez-Becker & Chiang, 2011); in this case the inner hole (or gap) is created by the tidal effect of a planet within the hole and dust filtration at the inner edge of the outer disc is invoked to reduce the opacity of the inner disc. However, such models are at an early stage of development and is not clear what kind of planetary system would be required to match the accretion rates and spectral energy distributions in these systems.

Using the photoevaporation theory developed in the previous sections we can delineate the region of transition disc parameter space within which we expect objects created by photoevaporation to lie for stars with $M_{*} < 1.5M_{\odot}$ (This exercise is similar to that undertaken by Owen et al. 2011b except that we have now extended the predictions to different stellar mass ranges and added new observational data points). Since the radial scale of the photoevaporative flow scales linearly with mass, the radius at which the gap opens will obviously scale linearly with mass too. Furthermore, since the gap opens when the accretion rate falls below the

photoevaporation rate, then stellar mass effects are not important in the determining the accretion rates of transition discs other than through the implicit stellar mass dependence of the X-ray luminosity (and hence photoevaporation rate).

In Figure 17 we show the region in which photoevaporating transition discs are expected, over-plotted with observations⁸ of discs classified as transition discs: cyan triangles (Brown et al. 2009); blue filled triangles & squares (Cieza et al. 2010); black open squares (Ercolano et al. 2009); black filled squares (Espaillat et al. 2008,2010); black open circles (Hughes et al. 2009, 2010); red filled circles (Kim et al. 2009); magenta filled diamonds (Merin et al. 2010); green filled star (Najita et al. 2010). We note that as Cieza et al. (2010) do not fit for an inner hole radius but rather list the *Spitzer* band of the inner hole. Therefore, we split the sample into two: the objects with a $\lambda_{\text{turnoff}} \leq 5.8 \mu\text{m}$, the inner hole is conservatively set to be less than 5AU, for $\lambda_{\text{turnoff}} = 8 \mu\text{m}$ we again conservatively set an inner hole of 10AU (since the inner-hole must occur in the temperature range $\lambda = 8 - 24 \mu\text{m}$), we add that these are safe overestimates based on simple temperature structures of protoplanetary discs. It is also worth noting that at very low masses ($\sim 0.1M_{\odot}$) Ercolano et al. (2009) showed that current observations cannot determine the presence of holes smaller than $\sim 1 \text{ AU}$, due to a lack of contrast between the disc and the stellar photosphere.

The photoevaporation region is constructed by using the fact the photoevaporation profile is self-similar when the radius is scaled in terms of R_g . (i.e. if the gap opens at 1AU around a $1M_{\odot}$ star it would open at 0.1AU around a $0.1M_{\odot}$ star) and we use a X-ray luminosity scaling of $L_X \propto M_*^{3/2}$ (Preibisch et al. 2005, Guedel et al. 2007) to extend the region calculated by Owen et al. (2011b) to the full mass range. Again this shows that the observations can be separated into two groups, those with small inner-holes $\leq 20\text{AU}$ and small accretion rates $\leq 10^{-8} M_{\odot} \text{ yr}^{-1}$ that are consistent with a photoevaporative origin, and those discs with large accretion rates and large holes that cannot have a photoevaporative origin.

7.1.1 Role of stellar mass

Kim et al. (2009) noted that ‘transition’ discs may show correlations between disc properties and stellar mass. Within the X-ray photoevaporation framework, such correlation will be primarily driven by the variation of the X-ray luminosity with stellar mass ($L_X \propto M_*^{3/2}$; Preibisch et al. 2005, Guedel et al. 2007). In order to assess the role stellar mass may play in driving correlations between ‘transition’ disc properties, we have extended the population synthesis study performed in Owen et al. (2011b) to lower ($0.1M_{\odot}$) and higher ($1M_{\odot}$) masses, where we adopt an initial disc mass that scales linearly with stellar mass. Furthermore, as the scaling of the initial viscous time with stellar mass is unconstrained (see

⁸ Several other types of astrophysical objects are found to enter these samples (e.g. AGB star or debris discs): in these cases we follow the definitions of the authors and only plot objects that are classified as protoplanetary discs with a gap/hole in its dust disc.

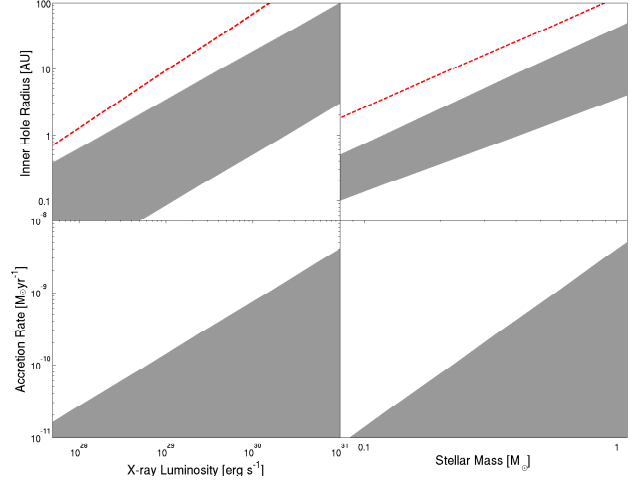


Figure 18. Panels showing the predicted regions occupied by transition discs created by photoevaporation. The shaded region represents the parameter space occupied by accreting transition discs (i.e. those with $\dot{M}_* > 1 \times 10^{-11} M_{\odot} \text{ yr}^{-1}$), the dashed line represents the maximum radius a transition disc may reach (even when a non-accreting transition disc) before ‘thermal sweeping’ sets in.

Section 8.1), we perform runs where $t_{\nu} \propto M_*$ and $t_{\nu} \propto M_*^{-1}$, although the results shown are only mildly sensitive to the chosen scaling.

In Figure 18 we show the predicted regions that the inner hole radius and accretion rates of transition discs occupy as a function of X-ray luminosity and stellar mass, both for accreting transition discs ($\dot{M}_* > 1 \times 10^{-11} M_{\odot} \text{ yr}^{-1}$), and non-accreting transition discs before ‘thermal sweeping’ sets in. In all cases they show strong positive correlations, driven by the radial scaling of the photoevaporating region with mass ($R_g \propto M_*$), and the positive correlation between mass and X-ray luminosity. The shaded regions are calculated by randomly sampling in time the disc during the transition phase, and represent the area populated by all transition discs through the entire population’s evolution. Thus, the correlations may vary with time for individual clusters, as only a certain fraction of discs will be in the transition disc phase at that point in time.

7.2 Relic Discs

As discussed in Section 6 we have uncovered a further phase in disc dispersal, i.e. the rapid removal of disc material due to what we term ‘thermal sweeping’. This phase begins at the point that the bound X-ray heated gas just inward of the inner disc rim becomes geometrically thick and when this gas starts to flow predominantly vertically, thus allowing further X-ray penetration in the disc mid-plane. The population synthesis calculation carried out in Owen et al. (2011b) of solar type stars ($M_* = 0.7M_{\odot}$) did not include this effect and therefore predicted the existence of long lived relic discs, for a small fraction of the total population. These were discs with very large inner holes $R > 100\text{AU}$ and low photoevaporation rates; for objects with the lowest X-ray luminosities these relics were estimated to remain for 10Myr and Owen et al. (2011b) argued that such discs might well correspond to some sources that had previously been classified as young

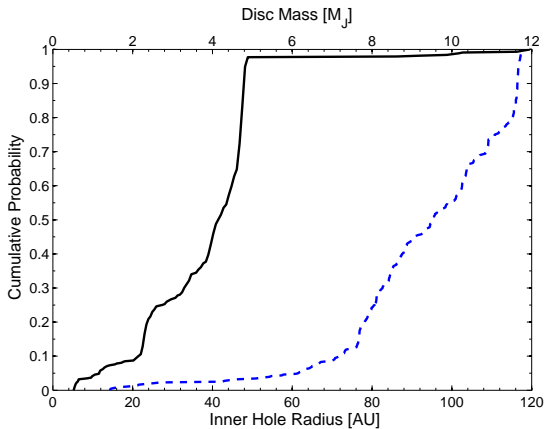


Figure 19. Cumulative distribution of inner hole radii (solid line) and disc mass (dashed line) at which the thermal sweeping process starts for the disc models calculated in the Owen et al. (2011b) population synthesis model ($0.7M_{\odot}$ stars).

(gas free) debris discs. This new thermal sweeping effect now provides a mechanism for the removal of these relic discs on a rapid (dynamical) time-scale ($\sim 10^3\text{--}4$ years).

In order to investigate at what point we expect the thermal sweeping to set in for the case of discs around higher mass stars (the calculations reported in Section 6 were for stars of mass $0.1M_{\odot}$) we apply the pressure criterion derived in Equation 15, since this corresponds to the point at which the radial width of the X-ray heated bound gas is $\sim H$. We follow the population synthesis approach of Owen et al. (2011b), i.e. we assume that all discs evolve according to a viscous similarity solution with fixed parameters and where the only quantity that varies from star to star is the X-ray luminosity which sets the photoevaporation rate. Then each star-disc system is evolved under the combined effects of viscous evolution and photoevaporation, following each system through the phase of gap opening and outer disc clearing. We identify the point that ‘thermal sweeping’ sets in with point that the maximum mid-plane pressure in the viscous disc falls below the value given by Equation 15. The variation of this radius with X-ray luminosity is rather modest, given that X-ray luminosity affects the radial profile of the clearing disc only through the mild effect of the degree of depletion of the disc during the phase of photoevaporation starved accretion (Drake et al. 2009; Owen et al. 2011b). Consequently our population synthesis model predicts that in the higher mass stars, thermal sweeping should set in at a narrow range of radii around 40 AU and disc masses $\lesssim 10M_J$ (see Figure 19).

Furthermore, the identification of this gas expulsion method significantly alters the ratios of accreting/non-accreting ‘transition’ discs expected, since discs spend less time in the non-accreting phase than previously expected. In Figure 20 we plot (as a function of X-ray luminosity) the fraction of the disc’s lifetime that the disc spends as a transition disc (crosses) and as a non-accreting transition disc (dots). This indicates that discs with high ($\gtrsim 10^{30}$ erg s^{-1}) and low ($\lesssim 10^{29}$ erg s^{-1}) X-ray luminosities spend the majority of their transition phase as accreting objects. Discs

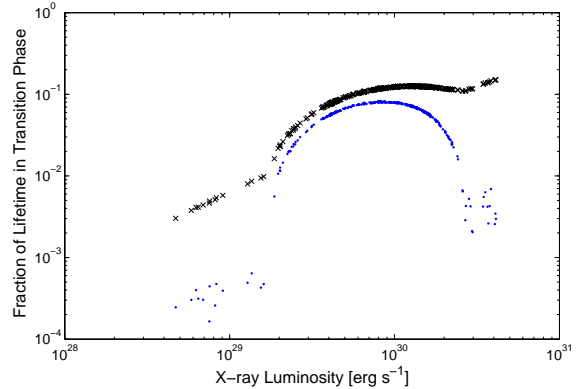


Figure 20. Fraction of the disc’s total lifetime that the disc presents as a transition disc (crosses) and a non-accreting transition disc (dots) as a function of X-ray luminosity.

with intermediate X-ray luminosities spend similar amounts of time in the accreting and non-accreting phases. Thus over the entire population of discs, one would expect most transition discs to appear as accreting. We can understand the relative lack of non-accreting transition discs at both high and low X-ray luminosity as follows. At low X-ray luminosity the disc accretes most of its mass onto the star over its longer lifetime, so that the mid-plane pressure is low once it enters the accreting phase and thermal sweeping sets in rather promptly. At high X-ray luminosity the process of photoevaporation starved accretion (Drake et al. 2009; Owen et al. 2011b) is vigorous and once the disc enters the clearing phase the outer disc is very depleted of gas (compared to the result of pure viscous evolution). Again the mid-plane pressure is low and the disc enters the thermal sweeping phase quickly.

The reason that such thermal sweeping was not seen in our previous hydrodynamic simulations of these more massive stars (Owen et al 2010) is that our hydrodynamical calculations of discs with inner holes used input disc profiles that were simply those of primordial discs truncated at a given value and did not take into account the fact that the outer disc profile would have been modified by viscous evolution and photoevaporation. The discs modelled thus had higher pressures than discs that had been self-consistently evolved and were thus less prone to thermal sweeping. This is in contrast to the sequence of disc clearing for a $0.1 M_{\odot}$ star (see Figure 12) in which the evolution of the disc profile is followed self-consistently in the hydrodynamic calculation. We emphasise that our estimate that the disc is rapidly cleared in higher mass ($0.7 M_{\odot}$) stars once the hole grows to 40 AU is very approximate given that it is not based on self-consistent hydrodynamical simulation of disc clearing in this case.

8 DISCUSSION

In this work we have indicated that one of the inescapable consequences of X-ray heating of a protoplanetary disc is a vigorous photoevaporative flow. The mass-loss rate is effectively determined by the X-ray luminosity only (when $L_X/L_{FUV} > 0.01$), with disc structure and stellar mass only

having weak effect on the resultant flow structure. This is easily understood in terms of the model presented in Section 2, where the conditions at the sonic surface are determined by the X-ray physics alone, so the disc below has to simply adjust to feed the sonic surface with the correct mass-flux. The consequence of such large mass-loss rates are that photoevaporation will be competing with accretion over much of the disc bearing life of young stars. Stars with higher X-ray luminosities will begin losing their discs first, followed by the lower X-ray luminosities stars at late times. Such an evolution is consistent with the observation that disc-less stars are systematically more X-ray luminous than stars still surrounded by discs (Neuhauser et al 1995; Stelzer & Neuhauser 2001; Flaccomio et al. 2003; Preibisch et al. 2005).

We have shown it is extremely unlikely that the EUV irradiation field plays any role in setting the photoevaporation rates: in any scenario where the EUV can reach the disc then so can the X-rays and the resulting X-ray driven wind is optically thick to the EUV. We have also set out arguments (backed up by simple toy FUV heating models) that FUV heating becomes important only below the X-ray sonic surface⁹. Only when the X-ray luminosity drops to sufficiently low ($L_X/L_{\text{FUV}} < 0.01$) values does the FUV begin to shut off the X-ray flow, and may possibly drive a flow itself. This result raises the intriguing possibility that what determines the evolution of a disc (and presumably its ability to form planets) is the star's intrinsic X-ray luminosity, rather than any variations in initial conditions when the star/disc system was created (Armitage 2011).

8.1 Disc lifetimes as a function of stellar mass

Since we have shown that the photoevaporation rate is independent of stellar mass (at fixed L_X) then, given some knowledge of the statistical dependence of X-ray luminosity on stellar mass and of the scaling of disc viscous parameters with stellar mass, we can examine the predicted relationship between disc lifetime and stellar mass. To this end we adopt the 'null' disc evolution method (Ercolano & Clarke 2010; Owen et al. 2011b), i.e. we assume that discs evolve in a pure viscous manner until the accretion rate equals the photoevaporative wind rate. At this point the disc is cleared rapidly and we define this point as the disc lifetime. For a disc in which $\nu \propto R$ the viscous similarity solutions (Lynden-Bell & Pringle, 1974) tell us:

$$\dot{M}_*(t) = \dot{M}_*(0) \left(1 + \frac{t}{t_\nu}\right)^{-3/2} \quad (18)$$

where t_ν is the disc's *initial* viscous time-scale (which, for the assumed linear scaling of viscosity with radius) is itself just proportional to the disc initial radius (R_1). Thus we can simply write the disc life-time (τ_d), when $t > t_\nu$ as:

$$\tau_d \propto \dot{M}_*(0)^{2/3} \dot{M}_w^{-2/3} t_\nu \quad (19)$$

⁹ This is not to say that FUV heating is then irrelevant to setting the structure of the warm disc at intermediate heights (Gorti & Hollenbach 2008, 2009), but merely that is not the determinant of the mass-loss rate.

Now using the fact $M_d(0)/\dot{M}_*(0) \propto t_\nu$ and $\dot{M}_w \propto L_X$ we find

$$\tau_d \propto M_d(0)^{2/3} L_X^{-2/3} t_\nu^{1/3} \quad (20)$$

Observations and theoretical work that suggest the discs enter this viscous phase after a self-gravitating phase suggest that $M_d(0) \propto M_*$, Furthermore X-ray observations (Guedel et al. 2004, Preibisch et al. 2007, Albacete Colombo et al. 2007) indicate that $L_X \propto M_*^{3/2-5/3}$, adopting $L_X \propto M_*^{3/2}$ we find that:

$$\tau_d \propto M_*^{-1/3} t_\nu^{1/3} \quad (21)$$

Unfortunately the scaling of t_ν (or equivalently R_1) with stellar mass is unknown. Some suggested scalings have been motivated by a wish to reproduce the claimed quadratic dependence of accretion rate on stellar mass (although it is likely that this empirical correlation - Natta et al. 2006 - may be largely driven by a mixture of sensitivity and selection effects: see Clarke & Pringle 2006, Tilling et al. 2008). One prescription that yields this quadratic dependence is that of Alexander & Armitage (2006), who assume that most observed discs are at an age that is much less than their initial viscous time-scale. Under this circumstance, the accretion rate is simply linked to the ratio of initial disc mass to initial viscous time-scale; a quadratic scaling of accretion rate on stellar mass then demands that (assuming $M_d(0) \propto M_*$) the initial viscous time-scale $t_\nu \propto 1/M_*$. If this were true, then Equation 21 would imply that disc lifetime scaled as $M_*^{-2/3}$. There are however a range of other possibilities based on reproducing the claimed accretion rate versus stellar mass relation: e.g. if $M_d(0) \propto M_*^2$ and t_ν is independent of stellar mass (as proposed by Dullemond et al. 2006) then $\tau_d \propto M_*^{1/3}$, while if we adopt $M_d(0) \propto M_*$ and now assume instead that discs are observed at times $\gg t_\nu$ then we would require $t_\nu \propto M_*^2$ in which case we again obtain $\tau_d \propto M_*^{1/3}$.

Clearly our estimates are resulting in a range of dependences none of which has a strong stellar mass dependence. Given the form of Equation 21, we see that a strong dependence of dispersal time-scale on stellar mass could only result if the initial disc viscous time-scale were an *extremely* strong function of stellar mass. This would appear to be unlikely, both because there are no obvious theoretical reasons to invoke such a strong mass dependence and also because such a strong dependence would imply a large stellar mass dependence of the relative numbers of stars observed with discs that are a substantial fraction of the mass of the central star.

8.2 Model Uncertainties

It is worth spending some time dwelling on some of the uncertainties and possible sources of error in a direct application of the model to real objects. These can be divided into two categories: (i) assumptions that directly affect the calculated mass-loss rates; (ii) how the mass-loss rates affect disc evolution.

8.2.1 Uncertainties in mass-loss rates

The analysis presented in Section 2 suggests that the mass-flux through the sonic surface is dominated by gas with temperatures around 2000 – 5000K. At these temperatures, molecular cooling (which we neglected in the X-ray thermal calculation used here, which just consider line cooling) could in principle be important (Glassgold et al. 2004; Meijerink et al. 2008; Gorti & Hollenbach 2008, 2009). In order to assess whether this is in fact the case (given that the densities at the sonic point are many orders of magnitude lower than those encountered in the preceding disc calculations) we need to estimate the relative contributions of the atomic line cooling at the sonic surface with that provided by molecules. From our calculations, the atomic line cooling is typically $\sim 10^{-13}$ erg cm $^{-3}$ s $^{-1}$ at 2000K. Given the density at the sonic surface ($\sim 10^6$ cm $^{-3}$), then molecular cooling would become important only if the CO abundance (X_{CO}) exceeded 0.1 at 2000K (using Equation C7 of Glassgold et al. 2004) which is many orders of magnitude higher than expected in discs (e.g. Bruderer et al. 2009). Thus we are confident that molecular cooling can be neglected at the sonic surface in photoevaporation calculations and hence the mass-loss rates will be unaffected.

While in this work and Owen et al. (2010) we went to great effort to indicate that the majority of factors that vary with time (e.g. disc structure, FUV/EUV luminosity) make very little difference to the derived mass-loss rate, we made an important assumption, namely the X-ray flux that is incident on the disc is an unvarying function of time. At first thoughts this is not a bad starting point since the time-averaged (X-ray variability due to flares are too fast to change a photoevaporative flow - Owen et al. 2011b) X-ray output of the star has been shown observationally to be fairly constant as a function of time (Guedel et al. 2004, Ingleby et al. 2011), crucially what is important to the photoevaporation model is not the X-ray output of the star but the ‘soft’ ($h\nu \lesssim 1\text{keV}$) X-ray luminosity visible to the disc.

Firstly, since most X-ray studies are concerned with the total X-ray luminosity of the objects (normally taken out to $h\nu \approx 10\text{keV}$), not much attention has been paid to the evolution of just the ‘soft’ component of the X-ray spectrum with time. While varying the amount of ‘hard’ X-ray irradiation will not affect the heating and hence photoevaporation rate, it will have an effect on the translation between observed X-ray luminosity of an object and the total ‘soft’ X-ray flux that reaches the disc.

A second factor is that various sources of absorbing column lie between the stellar corona and disc surface, for example: accretion columns, jets and (magnetic) disc winds may be present. Obviously if the absorbing column from these process approaches 10^{22}cm^{-2} then the X-rays will be screened from the disc and the mass-loss rates derived in the previous sections will be an overestimation of the actual photoevaporation rate. Thus, simply assuming that the disc sees an X-ray source with the same luminosity as the intrinsic X-ray luminosity may be an oversimplification, leading to an over estimate of the photoevaporation rates.

Finally, although we are confident about the magnitude of the X-ray photoevaporation, we cannot rule out the possibility that beyond 100 AU it is FUV photoevaporation that dominates the mass loss rate. This is because this is the

distance at which the X-rays and FUV fields heat the gas to comparable temperatures and where also such temperatures are comparable with the local escape temperature. Gorti & Hollenbach (2009) have suggested that this may be an important effect in truncating the disc at the outside (cf. a similar role for *external* FUV radiation in the case of the Orion proplyds Johnstone et al. 1998; Richling & Yorke, 2000; Adams et al 2004). Such truncation would influence the viscous evolution of the disc (Clarke 2007) by imparting a different boundary condition from the one adopted in the viscous calculations as noted by Gorti et al. 2009.

8.2.2 Uncertainties in disc evolution

Uncertainties in disc evolution *do not* affect the photoevaporation rates for a given stellar mass, X-ray luminosity and (where relevant) inner hole radius, given the insensitivity of these rates to the structure of the underlying disc. However it is the interplay between viscous evolution and photoevaporation that sets the sequence of gap opening and inner disc clearing. Viscous evolution sets the time-scale on which the gap opens and, by setting the mass remaining in the outer disc, also sets the time-scale of outer disc clearing.

Currently, the magnitude and even origin of the viscous processes in discs is not fully determined, nor the radial range within which various viscous processes are active (see Armitage 2011 for an up-to date review). Therefore, in order to determine the evolution of discs we adopt a similarity law put forward by (Lynden-Bell & Pringle, 1974) wherein $\nu \propto R$ since this crude assumption appears to be broadly compatible with observations of disc mass distributions and accretion rates in T Tauri stars (e.g. Hartmann et al. 1998).

Although the broad sequence of evolutionary phases outlined above is to be expected for any viscosity prescription, we are aware that there are quantitative effects that do depend on the magnitude and the radial dependence of the viscosity. In particular, we note that (as described in Section 7.1), the inner disc rapidly becomes optically thin following gap opening, as it becomes significantly dust depleted. Such a change will undoubtedly change the thermal and ionization structure of the disc. This in turn can be expected to affect the viscosity in the disc with consequences, for example, for the predictions we have made concerning the relative incidence of accreting vs non-accreting transition discs with a photoevaporative origin.

9 CONCLUSIONS

In this work we have outlined the basic properties of the photoevaporation of discs around low mass stars by the X-rays from the central star. In this regime, the photoevaporation rates are set by the properties in the X-ray flow and are fairly insensitive to variations in disc structure and extra heating sources e.g. FUV radiation. At the most basic level this indicates factors that determine discs’ lifetimes and evolution may stem from the stars’ intrinsic X-ray luminosities. Our main conclusions are summarised below:

- (i) The photoevaporative mass-loss rates are primarily set by the X-ray heating alone, as the sonic surface always occurs within the X-ray heated region. Extra UV heating provides little effect on the determined structure of the X-ray

wind and its associated sonic surface geometry and mass-loss rate if $L_X/L_{\text{FUV}} > 0.01$.

(ii) We have derived from first principles the scaling of photoevaporative mass loss from primordial discs with X-ray luminosity and stellar mass and have also derived analytical estimates of the total mass loss rates. The mass-loss rates scale approximately linearly with X-ray luminosity and have no explicit dependence on stellar mass. These scalings and absolute values have been confirmed through a large suite of numerical simulations.

(iii) We do not predict a strong dependence of disc lifetime on stellar mass for stars less massive than $1M_\odot$, in agreement with observations. Higher mass stars have higher X-ray luminosities but also have more massive discs to be dispersed. The resulting time-scale for disc dispersal would be a strong function of stellar mass only in the unlikely case that the viscous properties of discs were an extremely strong function of stellar mass.

(iv) We have explained why, in the case of discs with inner holes, the photoevaporative mass-loss rates scale linearly with X-ray luminosity and is independent of inner hole size and have calculated numerical models to calibrate the mass-loss rates.

(v) We find that once the mid-plane pressure of a disc with an inner hole drops below a critical value (given by Equations 15 & 16) the remaining disc is cleared rapidly (on a roughly dynamical time-scale). This process (which we have termed ‘thermal sweeping’) sets in once the layer of bound X-ray gas on the inside of the disc rim becomes thick (i.e. comparable with its vertical scale height) since at this stage the heated gas escapes preferentially normal to the disc plane and increases the exposure of the disc rim. Such rapid dispersal removes the possibility of the long lived ‘relic’ discs hypothesised in Owen et al. (2011b). We find that thermal sweeping sets in at around 10 – 15 A.U. in the case of low mass stars ($0.1M_\odot$) and we roughly estimate that the corresponding radius is $\lesssim 50$ AU for higher mass T Tauri stars ($\sim 0.7M_\odot$).

(vi) We find that when we take into account the spread in masses and X-ray luminosities of T Tauri stars, we can produce transition discs that span a wide range of properties (hole radii and accretion rate onto the star). In this way we can account for a large fraction ($\gtrsim 50\%$) of the observed transition discs. We cannot, however, account for large holes with high accretion rates (see Figure 17).

(vii) Photoevaporation and ‘thermal sweeping’ ultimately destroy the final disc, but it is still accretion onto the central star that removes most of the original disc mass ($\sim 10\% M_*$): in most cases only $\sim 10 - 20\%$ of the original disc mass lost through in the processes of photoevaporation or thermal sweeping.

ACKNOWLEDGEMENTS

We are grateful to the anonymous referee, whose comments helped improve this work. JEO acknowledges support of a STFC PhD studentship. This work was performed using the Darwin Supercomputer of the University of Cambridge High Performance Computing Service (<http://www.hpc.cam.ac.uk/>), provided by Dell Inc. using

Strategic Research Infrastructure Funding from the Higher Education Funding Council for England.

APPENDIX A: THE THEORY OF X-RAY PHOTOEVAPORATION: SCALING RELATIONS

In this appendix we develop the theory of X-ray photoevaporation from discs with a view to understanding how local quantities vary as a function of model input parameters. We make use of the fact that in thermal equilibrium the temperature of optically thin, X-ray heated gas is a roughly monotonic function of the ionisation parameter $\xi = L_X/nr^2$. In qualitative terms, the flow starts highly sub-sonically at the base of each streamline and is then accelerated by a mixture of pressure gradients and effective gravity, \mathbf{g}_{eff} (i.e. the combined effects of the gravity of the central star and a centrifugal term). It is assumed that viscous effects are negligible over the flow; thus the specific angular momentum of each fluid element is conserved, being at the Keplerian value at launch (cylindrical radius R_b) with value $h^2 = GM_* R_b$. Therefore,

$$\mathbf{g}_{\text{eff}} = -\frac{GM_*}{r^2}\hat{\mathbf{r}} + \frac{GM_*R_b}{R^3}\hat{\mathbf{R}} \quad (\text{A1})$$

where $\hat{\mathbf{r}}$, $\hat{\mathbf{R}}$ are unit vectors in the spherical radial and cylindrical radial directions.

In a steady state we can write the continuity equation in the form:

$$\frac{d\log\rho}{dl} = -\frac{d\log u}{dl} - \frac{d\log A}{dl} \quad (\text{A2})$$

(where l is a coordinate measured along the streamline and A represents the area of a streamline bundle, so that $d\log A/dl$ is simply the divergence of the unit vector along the streamline, $\hat{\mathbf{l}}$). This allows us to write the steady state momentum equation along a streamline in the form:

$$\left[\left(\frac{u}{c_s} \right)^2 - 1 \right] \frac{d\log u}{dl} = \frac{d\log A}{dl} - \frac{d\log c_s^2}{dl} + \frac{\mathbf{g}_{\text{eff}} \cdot \hat{\mathbf{l}}}{c_s^2} \quad (\text{A3})$$

Therefore a flow will undergo a sonic transition at the point where the right hand side of Equation A3 is equal to zero. In the special case of an isothermal flow, we would recover the result that in the absence of an external force ($g_{\text{eff}} = 0$) such a transition occurs at the point of transition from converging to diverging flow (the de Laval nozzle solution). Furthermore, in the case of spherical outflow under point mass gravity, the right hand side of Equation A3 yields the sonic condition of a Parker wind (Parker, 1958).

However, the present case is much more complicated, since we do not know the flow geometry *a priori*, because g_{eff} is non-negligible at all radii and because c_s is not constant. Although it is possible to solve for $u(l)$ (and hence $\rho(l)$ and $c_s(l)$) for a fixed streamline topology, there is no guarantee that such a solution would satisfy the steady state momentum equation perpendicular to the streamlines. We can use Equation A3 to write the condition for the sonic surface as:

$$c_s^2 = \frac{GM}{2R} \times \frac{R}{r} \times \frac{f_g}{f_A} \quad (\text{A4})$$

where

$$f_g = \frac{-\mathbf{g}_{\text{eff}} \cdot \hat{\mathbf{l}}}{GM/r^2} \quad (\text{A5})$$

and

$$f_A = \frac{\frac{d \log A}{d \tilde{l}} - \frac{d \log c_s^2}{d \tilde{l}}}{2/r} \quad (\text{A6})$$

The first two terms equate the temperature at the sonic surface to the usual expression for a spherical Parker wind; f_g takes into account of the different component of the effective force along the streamline compared with the Parker case (both due to the centrifugal term and the non-spherical geometry), while f_A takes into account the different divergence of non-spherical flows and also the fact the flow is non-isothermal. In thermal equilibrium the flow time-scale is long compared to any thermal time-scales and the derivative of the sound speed is small compared to the other terms (e.g. Adams et al. 2004). Furthermore, as the centrifugal force falls off rapidly with radius, f_A and f_g approach unity quickly (Begelman et al. 1983; Adams et al. 2004). Therefore provided the sonic surface is some distance from the base of the flow, the sound speed will be of order the Parker value.

At first look these remarks appear to preclude further analytic arguments, but in fact we can make useful progress by deriving *scaling relations*. First we consider the case where we have obtained a self-consistent steady state flow structure (via a hydrodynamical simulation) for a given set of input parameters, and we then change some parameter of the flow and obtain a new structure. We can then ask whether there are circumstances where one case is simply a scaled version of the original case.

If such a scaling does apply, then every streamline in the first case can be identified with a topologically identical streamline in the second case, which differs only in its overall geometrical scale. Such a scaling also implies that the variation of flow variables along each such streamline are scaled versions of each other, i.e. we write all variables in the form $u = u_0 \tilde{u}(\tilde{l})$ where \tilde{l} is the distance along the streamline scaled to the radius at the base of the streamline (R_b) and u_0 allows for a simple re-scaling of the velocity between the two streamlines. In this case we can write Equation A3 as:

$$\left[\left(\frac{u_0}{c_{s0}} \right)^2 \left(\frac{\tilde{u}}{\tilde{c}_s} \right)^2 - 1 \right] \frac{d \log \tilde{u}}{d \tilde{l}} = \frac{d \log \tilde{A}}{d \tilde{l}} - \frac{d \log \tilde{c}_s^2}{d \tilde{l}} + \frac{GM_*}{R_b c_{s0}^2} \frac{\tilde{\mathbf{g}}_{\text{eff}} \cdot \hat{\mathbf{l}}}{\tilde{c}_s^2} \quad (\text{A7})$$

where

$$\tilde{\mathbf{g}}_{\text{eff}} = -\frac{1}{\tilde{r}^2} \tilde{\mathbf{r}} + \frac{1}{\tilde{R}^3} \tilde{\mathbf{R}} \quad (\text{A8})$$

Now in order to obtain a consistent, self-similar solution we require that the above equation should contain only scaled variables (i.e. those denoted with a tilde) and should not depend on the parameters R_b , u_0 and c_{s0} which vary from one simulation to another. Examining the left hand side of Equation A7, we then require that $u_0 = c_{s0}$ (i.e. the Mach number of the flow is the same for the two scaled streamlines at given \tilde{l}).

We can furthermore argue that the individual values of u_0 and c_{s0} are the same for streamlines that are a scaled ver-

sion of each other: if c_{s0} were different then the temperature at given \tilde{l} would be different between the two streamlines (by a constant factor) and the density would also be necessarily different according to the parametrisation of temperature against ionisation parameter. Since this relation is not a simple power law scaling then the density variation along the streamlines would not be self-similar, in contradiction with our assumption. Therefore, for streamlines to map onto one another in a self-similar way, we must have the *same velocity and temperature structure* as a function of \tilde{l} .

Turning now to the right hand side of Equation A7 we see that in order that this does not contain variables that differ from case to case, we must have $R_{b0} \propto M_*$. Since the escape temperature is given by $T_{\text{esc}} \propto M_*/r$, this implies that T_{esc} is the same at given \tilde{l} for streamlines that map onto each other in a self-similar way, thus the importance of r_g as the natural scaling of the problem becomes clear.

A1 Primordial discs

We first consider the case of ‘primordial’ discs on the assumption that these are approximately scale free. Power law variation of mid-plane variables is an expectation of the Lynden-Bell & Pringle (1974) similarity solutions and appear to be consistent with observational estimates of disc surface density profiles which suggest that $\Sigma \propto R^{-1}$ (Andrews et al 2010). These would therefore appear to be good candidates for yielding self-similar solutions when the input parameters are varied, as the boundary conditions of the problem would be close to self-similar.

A1.1 Variation of L_X at constant M_*

We have seen above that strict self-similarity requires that $R_{b0} \propto M_*$. Thus if we vary L_X at fixed M_* , then R_{b0} is the same and each streamline simply maps onto a streamline with the same radius and with the same temperature and velocity variation along the streamline. Since the temperature is a function of ionisation parameter, it follows that as one varies L_X , the density scaling along each streamline must simply vary $\propto L_X$. The mass flux along each streamline is the product of stream-bundle area, velocity and density. As the former two are independent of L_X and the density scales with L_X , then the mass flux is simply $\propto L_X$.

Therefore, we conclude that primordial discs which differ only in their values of incident L_X should be topologically identical, with identical velocity and temperature structure, but with a mass weighting on each streamline that scales with L_X . This result agrees with the results of the hydrodynamical simulations of Owen et al (2011b) in which it was found that the mass loss rate scales linearly with L_X .

A1.2 Variation of M_* at constant L_X

In this case, the fact that $R_{b0} \propto M_*$ implies that variation of stellar mass should simply change the over-all radial scale of the flow (i.e. a streamline rooted at 10 A.U. in a simulation with $M = 1M_\odot$ should simply map on to a streamline rooted at 1 A.U. in the case of a simulation with $M = 0.1M_\odot$). As before, we require that the two scaled streamlines should have the same variation in velocity and temperature as a

function of distance along the streamline normalised to the radius of the streamline base, i.e. the same variation of ionisation parameter. Since $\xi = L_X/nr^2$, it follows that a radial scaling $\propto M_*$ results in a scaling with density of $\propto M_*^{-2}$. The mass-loss from the streamline is proportional to the product of the density ($\propto M_*^{-2}$), the local velocity (constant) and the area of the stream-bundle ($\propto M_*^2$): i.e. the mass loss rate along each streamline is the same as the mass loss rate over its scaled equivalent. Therefore (provided the disc is sufficiently radially extended that it encompasses the whole region from which significant mass loss occurs in all cases), we conclude that, at constant L_X , the mass flux in the wind is *independent*¹⁰ of M_* .

A2 Discs with inner holes

Here the truncated density profile of the disc introduces a particular radial scale (R_{hole}) to each underlying disc. However, if one fixes R_{hole} for a given mass, then the above arguments for L_X are still applicable. For fixed M_* and R_{hole} then as one varies L_X the density must also vary as $n \propto L_X$, resulting in a total mass-loss rate that varies linearly with X-ray luminosity. Furthermore, if one varies M_* , then one can simply map one solution with an inner hole radius to the equivalent inner hole around another mass using $R_{\text{hole}} \propto M_*$.

Neither of these cases however describe the situation that is normally of greatest interest i.e. the variation of photoevaporation rate with R_{hole} in the case of fixed M_* and L_X , which would allow us to compute the evolution of the mass loss rate as a disc is progressively cleared from the inside out. Since R_{hole} introduces a fixed scale into the problem no similarity solution exists than includes L_X , M_* and R_{hole} and it is not possible to analytically estimate such a scaling. Therefore, we defer a discussion of this case to Section 5 where our numerical results allow us to construct *a posteriori* an approximate scaling argument.

A3 Summary

We have shown that the flow from primordial discs is expected to be self-similar (when L_X and M_* are varied) and predict that the mass loss rate should scale linearly with L_X and be independent of M_* . Furthermore, we have shown that photoevaporation rates should scale linearly with L_X also in the case of discs with inner holes and that a disc with given inner hole radius can also be scaled to a different hole size ($\propto M_*$) when the stellar mass is varied. The flow topology is however not exactly self-similar in the case of discs with different hole sizes and fixed L_X and M_* . Given the lack of exactly scalable solutions in this case, we will return to this issue, using additional input from numerical solutions, in Section 5.

¹⁰ It is of course important to note, that even though there is no explicit mass dependence on photoevaporation rates from discs, there will of course be a strong implicit variation with mass through the variation of X-ray luminosity with stellar mass: observations suggest that $M_* \propto L_X^{3/2-5/3}$ (e.g. Preibisch et al. 2005, Guedel et al. 2007).

APPENDIX B: NUMERICAL FITS TO MASS-LOSS RATES

In this appendix, we provide fits to the total mass-loss rates and profiles obtained from the numerical calculations performed by Owen et al. (2010), Owen et al. (2011b) and in this work. The mass-loss profile fits were based on the results provided by the on-line ‘function finder’ provided at <http://zunzun.com>, and their functional form does *not* represent the results of analytic calculation and should be treated in such a way. Furthermore, these fits were performed in such a way as to described the cumulative mass-loss rates accurately which is important for the global viscous evolution. As such the fits are worst at small radius; should sensitivity at these radii become important more accurate fits to this region can be provided upon request. The surface mass-loss profiles $\dot{\Sigma}_w$ given in Equations B2 & B5 are provided in normalised form and must be scaled so that $\int 2\pi R \dot{\Sigma}_w dR$ yields the required total mass-loss rate, given in Equations B1 & B4.

B1 Primordial Discs

The total mass-loss rate variation with X-ray luminosity is shown in Figure 4, where the solid line is described by:

$$\dot{M}_w = 6.25 \times 10^{-9} \left(\frac{M_*}{1 M_\odot} \right)^{-0.068} \left(\frac{L_X}{10^{30} \text{ erg s}^{-1}} \right)^{1.14} M_\odot \text{ yr}^{-1} \quad (\text{B1})$$

The mass-loss profile, derived from the solid line in the left hand panel of Figure 4 in Owen et al. (2011b) is described by:

$$\begin{aligned} \dot{\Sigma}_w(x > 0.7) = & 10^{(a_1 \log_{10}(x)^6 + b_1 \log_{10}(x)^5 + c_1 \log_{10}(x)^4)} \\ & \times 10^{(d_1 \log_{10}(x)^3 + e_1 \log_{10}(x)^2 + f_1 \log_{10}(x) + g_1)} \\ & \times \left(\frac{6a_1 \log(x)^5}{x^2 \log(10)^7} + \frac{5b_1 \log(x)^4}{x^2 \log(10)^6} + \frac{4c_1 \log(x)^3}{x^2 \log(10)^5} \right. \\ & \left. + \frac{3d_1 \log(x)^2}{x^2 \log(10)^4} + \frac{2e_1 \log(x)}{x^2 \log(10)^3} + \frac{f_1}{x^2 \log(10)^2} \right) \\ & \times \exp \left[- \left(\frac{x}{100} \right)^{10} \right] \quad (\text{B2}) \end{aligned}$$

where $a_1 = 0.15138$, $b_1 = -1.2182$, $c_1 = 3.4046$, $d_1 = -3.5717$, $e_1 = -0.32762$, $f_1 = 3.6064$, $g_1 = -2.4918$ and:

$$x = 0.85 \left(\frac{R}{\text{AU}} \right) \left(\frac{M_*}{1 M_\odot} \right)^{-1} \quad (\text{B3})$$

where $\dot{\Sigma}_w(x < 0.7) = 0$. Logarithms of the form $\log(x)$ are taken taken using the natural base.

B2 Discs with Inner holes

As described previously we find that the total mass-loss rate is approximately independent of inner hole radius, which is approximately described by:

$$\dot{M}_w = 4.8 \times 10^{-9} \left(\frac{M_*}{1 M_\odot} \right)^{-0.148} \left(\frac{L_X}{10^{30} \text{ erg s}^{-1}} \right)^{1.14} M_\odot \text{ yr}^{-1} \quad (\text{B4})$$

The mass-loss profile, derived from the solid line in the right hand panel of Figure 4 in Owen et al. (2011b) is described

by:

$$\dot{\Sigma}_w(y) = \left[\frac{a_2 b_2 \exp(b_2 y)}{R} + \frac{c_2 d_2 \exp(d_2 y)}{R} + \frac{e_2 f_2 \exp(f_2 y)}{R} \right] \times \exp \left[- \left(\frac{y}{57} \right)^{10} \right] \quad (\text{B5})$$

where $a_2 = -0.438226$, $b_2 = -0.10658387$, $c_2 = 0.5699464$, $d_2 = 0.010732277$, $e_2 = -0.131809597$, $f_2 = -1.32285709$ and:

$$y = 0.95 (R - R_{\text{hole}}) \left(\frac{M_*}{1 M_{\odot}} \right)^{-1} \quad (\text{B6})$$

where $\dot{\Sigma}_w(y < 0) = 0$.

REFERENCES

- Adams, F. C., Hollenbach, D., Laughlin, G., & Gorti, U. 2004, *ApJ*, 611, 360
- Alexander, R. D., Clarke, C. J., & Pringle, J. E. 2004, *MNRAS*, 354, 71
- Alexander, R. D., Clarke, C. J., & Pringle, J. E. 2005, *MNRAS*, 358, 283
- Alexander, R. D., Clarke, C. J., & Pringle, J. E. 2006, *MNRAS*, 369, 216
- Alexander, R. D., Clarke, C. J., & Pringle, J. E. 2006, *MNRAS*, 369, 229
- Alexander, R. D., & Armitage, P. J. 2006, *ApJL*, 639, L83
- Alexander, R. D., & Armitage, P. J. 2009, *ApJ*, 704, 989
- Andrews, S. M., & Williams, J. P. 2005, *ApJ*, 631, 1134
- Andrews, S. M., & Williams, J. P. 2007, *ApJ*, 671, 1800
- Andrews, S. M., Wilner, D. J., Hughes, A. M., Qi, C., & Dullemond, C. P. 2010, *ApJ*, 723, 1241
- Armitage, P. J., & Hansen, B. M. S. 1999, *Nature*, 402, 633
- Armitage, P. J. 2010, arXiv:1011.1496
- Begelman, M. C., McKee, C. F., & Shields, G. A. 1983, *ApJ*, 271, 70
- Brown, J. M., Blake, G. A., Qi, C., Dullemond, C. P., Wilner, D. J., & Williams, J. P. 2009, *ApJ*, 704, 496
- Bruderer S., Doty S. D., Benz A. O., 2009, *ApJS*, 183, 179
- Calvet, N., D'Alessio, P., Hartmann, L., Wilner, D., Walsh, A., & Sitko, M. 2002, *ApJ*, 568, 1008
- Calvet, N., et al. 2005, *ApJL*, 630, L185
- Cieza, L. A., et al. 2010, *ApJ*, 712, 925
- Clarke, C. J., Gendrin, A., & Sotomayor, M. 2001, *MNRAS*, 328, 485
- Clarke, C. J., & Pringle, J. E. 2006, *MNRAS*, 370, L10
- Clarke, C. J. 2007, *MNRAS*, 376, 1350
- D'Alessio, P., Canto, J., Calvet, N., & Lizano, S. 1998, *ApJ*, 500, 411
- D'Alessio, P., Calvet, N., Hartmann, L., Lizano, S., & Cantó, J. 1999, *ApJ*, 527, 893
- D'Alessio, P., Calvet, N., & Hartmann, L. 2001, *ApJ*, 553, 321
- Drake, J. J., Ercolano, B., Flaccomio, E., & Micela, G. 2009, *ApJL*, 699, L35
- Dullemond, C. P., & Dominik, C. 2005, *A&A*, 434, 971
- Dullemond, C. P., Natta, A., & Testi, L. 2006, *ApJL*, 645, L69
- Dutrey, G., Guilloteau, S., Ménard, F., Simon, M., & Dutrey, A. 2000, *A&A*, 355, 165
- Ercolano, B., Barlow, M. J., Storey, P. J., & Liu, X.-W. 2003, *MNRAS*, 340, 1136
- Ercolano, B., Barlow, M. J., & Storey, P. J. 2005, *MNRAS*, 362, 1038
- Ercolano, B., Drake, J. J., Raymond, J. C., & Clarke, C. C. 2008, *ApJ*, 688, 398
- Ercolano, B., Clarke, C. J., & Drake, J. J. 2009, *ApJ*, 699, 1639
- Ercolano, B., Clarke, C. J., & Robitaille, T. P. 2009, *MNRAS*, 394, L141
- Ercolano, B., & Clarke, C. J. 2010, *MNRAS*, 402, 2735
- Ercolano, B., & Owen, J. E. 2010, *MNRAS*, 406, 1553
- Ercolano, B., Clarke, C. J., & Hall, A. C. 2011, *MNRAS*, 410, 671
- Ercolano, B., Bastian, N., Spezzi, L., & Owen, J. 2011, *MNRAS*, 986
- Espaillet, C., et al. 2008, *ApJL*, 689, L145
- Espaillet, C., et al. 2010, *ApJ*, 717, 441
- Flaccomio, E., Micela, G., & Sciortino, S. 2003, *A&A*, 402, 277
- Font, A. S., McCarthy, I. G., Johnstone, D., & Ballantyne, D. R. 2004, *ApJ*, 607, 890
- Furlan, E., Luhman, K. L., Espaillet, C., et al. 2011, *ApJS*, 195, 3
- Gorti U., Hollenbach D., 2004, *ApJ*, 613, 424
- Gorti, U., & Hollenbach, D. 2008, *ApJ*, 683, 287
- Gorti, U., & Hollenbach, D. 2009, *ApJ*, 690, 1539
- Gorti, U., Dullemond, C. P., & Hollenbach, D. 2009, *ApJ*, 705, 1237
- Güdel, M. 2004, *A&A Rev*, 12, 71
- Güdel, M., et al. 2007, *A&A*, 468, 353
- Haisch, K. E., Jr., Lada, E. A., & Lada, C. J. 2001, *ApJL*, 553, L153
- Hartigan, P., Edwards, S., & Ghandour, L. 1995, *ApJ*, 452, 736
- Hartmann, L., Calvet, N., Gullbring, E., & D'Alessio, P. 1998, *ApJ*, 495, 385
- Hayes, J. C., Norman, M. L., Fiedler, R. A., Bordner, J. O., Li, P. S., Clark, S. E., ud-Doula, A., & Mac Low, M.-M. 2006, *ApJS*, 165, 188
- Hollenbach, D., Johnstone, D., Lizano, S., & Shu, F. 1994, *ApJ*, 428, 654
- Hughes, A. M., et al. 2009, *ApJ*, 698, 131
- Hughes, A. M., et al. 2010, *AJ*, 140, 887
- Ingleby, L., Calvet, N., Hernández, J., Briceño, C., Espaillet, C., Miller, J., Bergin, E., & Hartmann, L. 2011, *AJ*, 141, 127
- Johnstone, D., Hollenbach, D., & Bally, J. 1998, *ApJ*, 499, 758
- Kim, K. H., et al. 2009, *ApJ*, 700, 1017
- Krauss, O., Wurm, G., Mousis, O., Petit, J.-M., Horner, J., & Alibert, Y. 2007, *A&A*, 462, 977
- Landau, L. D., & Lifshitz, E. M. 1987, *Fluid Mechanics: Volume 6 (Course of Theoretical Physics)*, A Butterworth-Heinemann Title; 2nd Edition, 1987
- Liffman, K. 2003, *PASA*, 20, 337
- Luhman, K. L., Allen, P. R., Espaillet, C., Hartmann, L., & Calvet, N. 2010, *ApJS*, 186, 111
- Lynden-Bell, D., & Pringle, J. E. 1974, *MNRAS*, 168, 603
- Mamajek, E. E. 2009, *American Institute of Physics Conference Series*, 1158, 3
- Merín, B., et al. 2010, *ApJ*, 718, 1200

- Muzerolle, J., Allen, L. E., Megeath, S. T., Hernández, J., & Gutermuth, R. A. 2010, *ApJ*, 708, 1107
- Najita, J. R., Strom, S. E., & Muzerolle, J. 2007, *MNRAS*, 378, 369
- Najita, J. R., Carr, J. S., Strom, S. E., Watson, D. M., Pascucci, I., Hollenbach, D., Gorti, U., & Keller, L. 2010, *ApJ*, 712, 274
- Neuhaeuser, R., Sterzik, M. F., Schmitt, J. H. M. M., Wichmann, R., & Krautter, J. 1995, *A&A*, 297, 391
- Owen, J. E., Ercolano, B., Clarke, C. J., & Alexander, R. D. 2010, *MNRAS*, 401, 1415
- Owen, J. E., Ercolano, B., & Clarke, C. J. 2011, *MNRAS*, 411, 1104
- Owen, J. E., Ercolano, B., & Clarke, C. J. 2011, *MNRAS*, 412, 13
- Pascucci, I., & Sterzik, M. 2009, *ApJ*, 702, 724
- Pascucci, I., et al. 2011, *ApJ*, 736, 13
- Parker, E. N. 1958, *ApJ*, 128, 664
- Perez-Becker, D., & Chiang, E. 2011, *ApJ*, 735, 8
- Preibisch, T., et al. 2005, *ApJS*, 160, 401
- Richling, S., & Yorke, H. W. 1997, *A&A*, 327, 317
- Richling, S., & Yorke, H. W. 1998, *A&A*, 340, 508
- Richling, S., & Yorke, H. W. 2000, *ApJ*, 539, 258
- Shu, F. H., Johnstone, D., & Hollenbach, D. 1993, *Icarus*, 106, 92
- Skrutskie, M. F., Dutkevitch, D., Strom, S. E., Edwards, S., Strom, K. M., & Shure, M. A. 1990, *AJ*, 99, 1187
- Stelzer, B., & Neuhäuser, R. 2001, *A&A*, 377, 538
- Strom, K. M., Strom, S. E., Edwards, S., Cabrit, S., & Skrutskie, M. F. 1989, *AJ*, 97, 1451
- Suzuki, T. K., & Inutsuka, S.-i. 2009, *ApJL*, 691, L49
- Tilling, I., Clarke, C. J., Pringle, J. E., & Tout, C. A. 2008, *MNRAS*, 385, 1530
- Yasui, C., Kobayashi, N., Tokunaga, A. T., Saito, M., & Tokoku, C. 2009, *ApJ*, 705, 54
- Yorke, H. W., & Welz, A. 1996, *A&A*, 315, 555